Energy Calibration of the *BaBar* EMC Using the π^0 Invariant Mass Method

David J. Tanner

October 1998

THE UNIVERSITY
of MANCHESTER

High Energy Group

Department of Physics and Astronomy

Contents

List of Figures

List of Tables

Abstract

The *BaBar* electromagnetic calorimeter energy calibration method was compared with the local and global peak iteration procedures, of Crystal Barrel and CLEO-II. An investigation was made of the possibility of $\Upsilon(4S)$ background reduction, which could lead to increased statistics over a shorter time interval, for efficient calibration runs. The *BaBar* software package was used with unreconstructed data to study the energy response of the calorimeter, by utilising the π^0 mass constraint on pairs of photon clusters.

Acknowledgements

Thanks firstly go to my supervisor Roger Barlow, for his constant help, guidance and supervision. I would also like to thank Fred Loebinger, for listening to my crazy ideas. The Manchester HEP group has been particularly helpful, notably the Manchester *BaBar* Colla-beer-ation: Jim, Jon, Andy, Elias, Nick and the honourary member John K.

A "thousand thank-yous" must also be given to: Helmut Marsiske, Brian Heltsey, Phil Strother, Sasha Bukin, and my Edinburgh colleague Ste Gowdy, who is almost too helpful.

Last but not least, I would like to thank my parents for putting up with me for a year. This thesis would not have been possible without their encouragement and support.

Dave "Gone for a π^{nt}" Tanner

Declaration

No portion of the work referred to in this thesis has been submitted in support of an application for another degree or qualification of this or any other university or other institute of learning.

Copyright in text of this thesis rests with the Author. Copies (by any process) either in full, or of extracts, may be made **only** in accordance with instructions given by the Author and lodged in the John Rylands University Library of Manchester. Details may be obtained from the Librarian. This page must form part of any such copies made. Further copies (by any process) of copies made in accordance with such instructions may not be made without the permission (in writing) of the Author.

The ownership of any intellectual property rights which may be described in this thesis is vested in the University of Manchester, subject to any prior agreement to the contrary, and may not be made available for use by third parties without the written permission of the University, which will prescribe the terms and conditions of any such agreement.

Further information on the conditions under which disclosures and exploitation may take place is available from the Head of the Department of Physics and Astronomy.

Chapter 1

Introduction

In recent years, the formulation of the Standard Model has improved considerably our understanding of the elementary particles and their interactions. It is now known that nature has provided us with three distinct generations of quarks and leptons, whilst accomodating for the fundamental forces in the provision of a number of integer-spin gauge bosons. However, despite continued and unprecedented agreement between experimental observations and theoretical predictions, many unanswered questions still remain. For example, the exact mechanism of electroweak symmetry breaking, through which the quarks and leptons acquire their spectrum of masses is unknown; moreover, the origin of CP violation is not fully understood. Indeed, the unsatisfactory presence of eighteen undetermined free parameters in the Standard Model, coupled with the prominent absence of gravity, has forced many to conclude that our quantum field theories are only a low energy approximation to a grand, more 'unified' theory.

The Large Hadron Collider at CERN and the PEP-II facility at SLAC, operating at the high energy and higher luminosity frontiers respectively, will provide us with the invaluable opportunity to validate further the predictions of the Standard Model, or to probe the physics beyond.

1.1 The *BaBar* Experiment and *CP* Violation

An international collaboration is designing and constructing a multi-purpose detector for the *BaBar* Experiment, to fully exploit the physics potential and clean environment of the PEP-II asymmetric e^+e^- collider. One of the *BaBar* experiments principal aims is to study the weak decays of B mesons, where the exhibition of *CP* violation is expected to be large. Within the framework of the Standard Model, these effects can be incorporated through the introduction of a complex phase to the Cabibbo-Kobayashi-Maskawa quark mixing matrix [1]. This has fundamental implications for the subtle asymmetry between matter and anti-matter, which give rise to *CP* violation. Clear predictions result, which will be tested by *BaBar*.

1.2 Calibration and Monitoring

In order to achieve the targeted sensitivity, for measurements of asymmetry in important *CP* decay modes, and to ensure that very rare decay channels are observed, stringent requirements are placed on the performance of the *BaBar* detector. Since B meson decays frequently contain π^0's with photon energies below 100 MeV, a CsI(Tl) electromagnetic calorimeter with a high photon detection efficiency and excellent energy resolution is needed. Ensuring that the *BaBar* electromagnetic calorimeter system achieves and maintains the planned resolution in a potentially high radiation environment, demands an accurate and precise method of setting the energy scale. A variety of calibration and monitoring procedures are therefore planned. These will characterize the response of the detector for a range of physical processes. Events involving high and low energy particles, such as Bhabha scattering, radiative QED Bhabhas and muon pairs will be used. Importantly, the low energy region will be checked by constraining the energy of well-separated photon pairs, to the reconstructed π^0 mass in the neutral pion decay $\pi^0 \rightarrow \gamma\gamma$.

This calibration technique is expected to be useful for the 20 MeV to 1 GeV energy region, but could be flawed at the very lowest energies, where background effects are not negligible. Figure (1.1) displays the requirements for the optimization of photon detection efficiency, and excellent energy resolution at low energies. The detector performance was simulated using a detailed Monte Carlo program [19]. The reduction of this background could enable the extraction of calibration information, over a time scale adequate for short-term variations in the response of the system to be monitored. An investigation of this reduction will be one of the aims of this thesis.
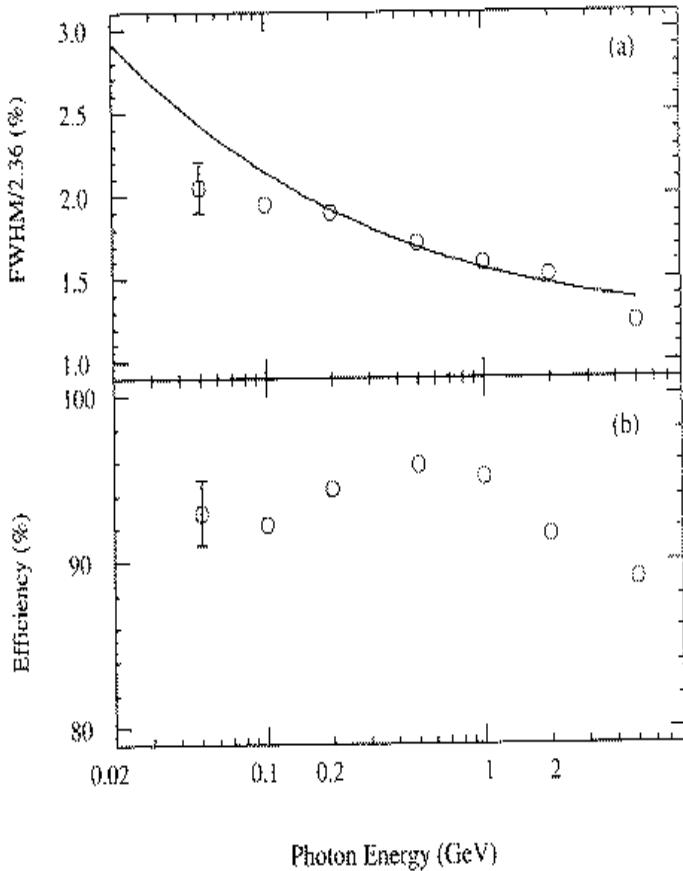
Figure 1.1: Energy resolution (a) and photon detection efficiency (b) requirements of the *BaBar* electromagnetic calorimeter. Displayed for $\cos\theta \rightarrow 0$ in the laboratory frame, solid line indicates target resolution.

Chapter 2

Theory

2.1   Physics Aims

The very early Universe may yet prove to be an important testing ground for speculative theories of particle physics. Even with current technology, the energy at which the intrinsic strength of the electroweak interaction is expected to become comparable to that of the strong, seems inescapably out of reach[1]. Nevertheless, the *BaBar* Experiment could provide a glimpse of the physical phenomena which occur at higher energies, through the independent determination of as many parameters as possible, in *CP* violating B decays. Such observations would enable the minimal Standard Model $(SU(3)_C \otimes SU(2)_L \otimes U(1)_Y)$ to be overconstrained, and therefore tested.

The elucidation of the origin of *CP* violation is of equal importance. It has been suggested that electroweak baryogenesis, resulting from the mixing of three generations of quarks, is unable to account satisfactorily for the observed baryon asymmetry of the Universe [3]. The ratio of the number of baryons to the number

---

[1] Current extrapolations at the GUT scale suggest that this unification may occur at a unification mass $\approx 10^{15}$ GeV.

of photons in our Universe, calculable from the baryon asymmetry of models based upon Grand Unified Theories, is *close* to the observed value.

$$\frac{n_B}{n_\gamma} \approx 10^{-9} \qquad (2.1)$$

An unexpected result for the measured value of the CKM complex phase, or any deviation from unitarity bounds would imply the existence of new sources of *CP* violation [4]. Thus, the inference of the higher-order presence of multi-Higgs, Supersymmetric particles or a fourth generation of quarks could provide an answer to the *CP* problem, and account for the overall preponderance of matter.

2.2   *CP* Violation

CP violation has been observed over thirty years ago in the decays of neutral kaons

$$\delta = \left|\frac{q}{p}\right|^2 = \frac{\Gamma(K_L \to \pi^- l^+ \nu) - \Gamma(K_L \to \pi^+ l^- \nu)}{\Gamma(K_L \to \pi^- l^+ \nu) + \Gamma(K_L \to \pi^+ l^- \nu)} \approx 3.3 \times 10^{-3} \qquad (2.2)$$

where K_S and K_L are the two mass eigenstates of the neutral K meson system:

$$|K_S> = p|K^0> + q|\bar{K}^0>, \quad |K_L> = p|K^0> - q|\bar{K}^0> . \qquad (2.3)$$

Here, S and L refer to the short and long relative lifetimes of the states; the coefficients p and q are complex numbers which define the K_S and K_L eigenstates of the non-Hermitian matrix operator.

The discovery of an unexpectedly long b quark lifetime at PEP in 1983 ($\tau_B \approx 10^{-12} s$), together with that of significant $B^0 - \bar{B}^0$ mixing shortly after, assured the future prospects of observing *CP* violation in the time-dependent asymmetries of B meson decays.

2.2.1 The Unitarity Triangle

The charge-raising current for the weak interaction[2]

$$J^\mu = \begin{pmatrix} \bar{u} & \bar{c} & \bar{t} \end{pmatrix} \gamma_\mu \frac{(1-\gamma^5)}{2} V \begin{pmatrix} d \\ s \\ b \end{pmatrix} \tag{2.4}$$

contains the 3×3 CKM quark mixing matrix V.[3]

$$V = \begin{pmatrix} c_{12}c_{13} & s_{12}c_{13} & s_{13}e^{-i\delta} \\ -s_{12}c_{23} - c_{12}s_{13}s_{23}e^{i\delta} & c_{12}c_{23} - s_{12}s_{23}s_{13}e^{i\delta} & s_{23}c_{13} \\ s_{12}s_{23} - c_{12}c_{23}s_{13}e^{i\delta} & -c_{12}s_{23} - s_{12}c_{23}s_{13}e^{i\delta} & c_{23}c_{13} \end{pmatrix} \tag{2.5}$$

In the Standard Model, the CKM matrix relates the bases of the quark mass eigenstates and the weak eigenstates, which are not the same

$$\begin{pmatrix} d' \\ s' \\ b' \end{pmatrix} = \begin{pmatrix} V_{ud} & V_{us} & V_{ub} \\ V_{cd} & V_{cs} & V_{cb} \\ V_{td} & V_{ts} & V_{tb} \end{pmatrix} \begin{pmatrix} d \\ s \\ b \end{pmatrix}. \tag{2.6}$$

For six quarks, the matrix has three rotation angles and a complex phase $e^{i\delta}$. If the amplitudes for the weak processes are equivalent and real, then the existence of a complex phase would ensure that for a certain relative phase, *CP* violation can occur. The scenario for four quarks is completely generalised, however, because the third generation of quarks decouple. Mixing is then initiated by a single Cabibbo angle.

A more instructive parametrisation was due to Wolfenstein. Re-casting the Cabibbo $\sin\theta_c$ term (which couples the charged currents to *rotated* quark states) as λ, then $\cos\theta_c \approx 1 - \frac{\lambda^2}{2}$ and up to $O(\lambda^3)$, the CKM matrix has the form

$$V = \begin{pmatrix} V_{ud} & V_{us} & V_{ub} \\ V_{cd} & V_{cs} & V_{cb} \\ V_{td} & V_{ts} & V_{tb} \end{pmatrix} \approx \begin{pmatrix} 1 - \frac{\lambda^2}{2} & \lambda & A\lambda^3(\rho - i\eta) \\ -\lambda & 1 - \frac{\lambda^2}{2} & A\lambda^2 \\ A\lambda^3(1 - \rho - i\eta) & -A\lambda^2 & 1 \end{pmatrix} \tag{2.7}$$

---

[2] And similarly for the Hermitian conjugate charge-lowering current.
[3] Here S_{ij} represents $\sin\theta_{ij}$ etc.

where A is a parameter which is dependent upon the b lifetime and other factors, and η is a complex parameter relating to the original phase. The unitarity of the CKM matrix dictates that the sum of the elements-squared in any row or column must equal unity:

$$\sum_{i=1}^{3} |V_{1i}|^2 \quad = \quad \sum_{i=1}^{3} |V_{2i}|^2 \quad = \quad \sum_{i=1}^{3} |V_{3i}|^2 \tag{2.8}$$

$$\Rightarrow V^\dagger V = I \tag{2.9}$$

Mixing and CP violation can be described in a similar way to the neutral kaon system, but any small violation of the unitarity constraints would give a significant contribution to $B - \bar{B}$ mixing. From the orthogonality of the first and third columns of the CKM matrix, the relation

$$V_{ud}V_{ub}^* + V_{cd}V_{cb}^* + V_{td}V_{tb}^* = 0 \tag{2.10}$$

can be represented as a triangle in an Argand diagram. Rescaling by a factor $V_{cb}^* \sin \theta_{12}$ and setting the cosines to one produces a triangle with an apex at the co-ordinate (ρ, η), and a base of unit length (Figure 2.1).
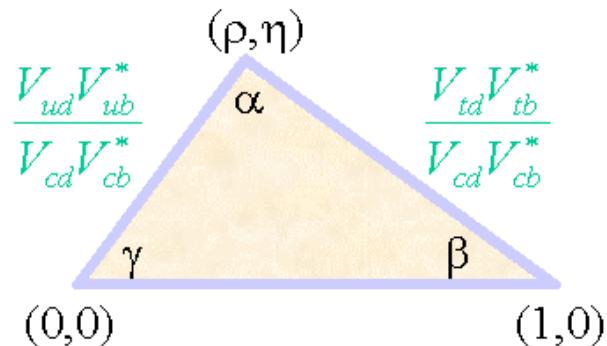
Figure 2.1: The rescaled Unitarity Triangle

2.2.2 *CP* Asymmetries in the B System

To overconstrain the Standard Model, it is essential to determine all of the angles and sides of the unitarity triangle. This can be accomplished by accurately measuring the asymmetry inherent in certain decay channels. In consideration of the decay $B_d^0 \to J/\psi K^{*0}(K^{*0} \to K_S^0 \pi^0)$, one can reliably extract a value for the angle β of the unitarity triangle[4].

The decay from which the angle α may be extracted, $B_d^0 \to \pi^+ \pi^-$, can occur through tree-level and higher-order penguin decays. The *CP* violating contributions from these orders have identical weak phase. Since the parameter ρ[5],

$$\rho = \frac{A_P}{A_T} \qquad (2.11)$$

relates the value of α to the observed asymmetry, the total penguin contribution to the decay must be evaluated[6]. If the *CP* asymmetry in $B_d^0 \to \pi^+ \pi^-$ is found to be small because ρ is small, then $\sin(2\alpha)$ may be measured accurately [6]. Weak interaction mixing is permitted between the $\bar{B}^0$ and the B^0, through second-order box diagrams (Figure 2.2).
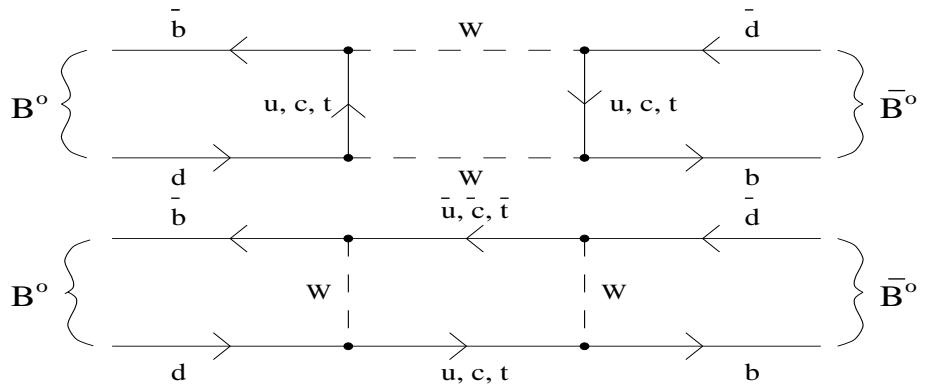
Figure 2.2: Box diagrams for B^0-$\bar{B}^0$ mixing

---

[4] Although, the best decay channel for extraction of the angle β is from $B_d^0 \to J/\psi K_S^0$
[5] ρ is the ratio of penguin (A_P) to tree (A_T) amplitudes
[6] The current data from CLEO suggest that ρ is in fact greater than one[5]. (Cabbibo suppression factors are not included in A_P and A_T)

Produced in a coherent state, the B^0 and $\bar{B}^0$ must be tagged as a flavour mode or a CP eigenstate, respectively.[7] Using the time t in the following equations, the time-dependence of the asymmetry can be reconstructed from the difference between the tagging mode and the decay CP eigenstate. Defining

$$\lambda_f \equiv \left(\frac{q_B}{p_B}\right)\frac{\bar{A}}{A}, \tag{2.12}$$

the decay rate for initially pure B^0 or $\bar{B}^0$ states to decay into a final CP eigenstate f, has the following time-dependence:

$$\Gamma(B^0(t) \to f) = |A|^2 e^{-\Gamma t}\left([1 + |\lambda_f|^2] \pm [1 - |\lambda_f|^2]\cos(\triangle Mt) \mp Im\lambda_f \sin(\triangle Mt)\right) \tag{2.13}$$

where the bottom sign is for $\bar{B}^0$ and the top for B^0. $\bar{A}$(A) is the decay amplitude to a CP eigenstate, f for $\bar{B}^0(B^0)$, and the q_B and p_B are defined in a similar manner to equations 2.3. The time-dependent CP asymmetry is given by the following

$$f(t) = \frac{\Gamma(B^0(t) \to f) - \Gamma(\bar{B}^0(t) \to f)}{\Gamma(B^0(t) \to f) + \Gamma(\bar{B}^0(t) \to f)} \tag{2.14}$$

$$f(t) = \frac{(1 - |\lambda|^2)\cos(\triangle Mt) - 2Im\lambda \sin(\triangle Mt)}{1 + |\lambda|^2}. \tag{2.15}$$

CP violation in mixing requires $\left|\frac{q}{p}\right| \neq 1$. If only one weak decay phase ϕ_D is present in the $b \to c\bar{c}s$ transition, then the ratio of the amplitudes is a pure phase

$$\frac{\bar{A}}{A} = e^{-2i\phi_D} = \frac{V_{cb}V_{cs}^*}{V_{cb}^*V_{cs}}. \tag{2.16}$$

Consequently, this asymmetry will determine the phase of the element $arg|V_{td}|$. If the amplitude for $B^0 \to f$ were the same as for $\bar{B}^0 \to f$, then CP would not be violated. It is the phase difference between decay amplitudes which is of importance here. Since a K_S is present in the final state, $K - \bar{K}$ mixing can occur. Interference due to

$$B^0(t) \to f, \qquad B^0(t) \to \bar{B}^0(t) \to f$$

---

[7]Or vice-versa.

must then be taken into account using

$$\lambda = \frac{q}{p}\frac{<f|\mathcal{H}|B^0>}{<f|\mathcal{H}|\bar{B}^0>} \equiv \left(\frac{q_B}{p_B}\right)\left(\frac{\bar{A}}{A}\right)\left(\frac{q}{p}\right)_K, \qquad \left(\frac{q}{p}\right)_K = \frac{V_{cs}V_{cd}^*}{V_{cs}^*V_{cd}}. \qquad (2.17)$$

Finally, the mixing phase, ϕ_M for the B_d^0 system is given by the ratio of the CKM vertex factors [7]

$$\left(\frac{q_B}{p_B}\right) = \frac{V_{tb}^*V_{td}}{V_{tb}V_{td}^*} = e^{-2i\phi_M} \qquad (2.18)$$

Putting these terms together,

$$\lambda(B_d^0 \to J/\psi K_S^{*0}) = \left(\frac{V_{tb}^*V_{td}}{V_{tb}V_{td}^*}\right)\left(\frac{V_{cb}V_{cs}^*}{V_{cb}^*V_{cs}}\right)\left(\frac{V_{cs}V_{cd}^*}{V_{cs}^*V_{cd}}\right) \qquad (2.19)$$

$$\Rightarrow Im\lambda = -\sin(2\beta) \qquad a_f(t) \propto \sin 2\beta \qquad (2.20)$$

To illustrate further, the measurement of asymmetry, $a_f(t)$ can be used to obtain the relative phase and magnitudes of the CKM matrix elements, through the direct extraction of the angle β. Decay channels such as $J/\psi K^{*0}$ are therefore of particular interest, because they demonstrate clearly the need for good π^0 reconstruction efficiency.

2.2.3 π^0 Resolution and Efficiency

To summarise, the following reasons specify the detector requirements, of high photon detection efficiency and excellent energy resolution in neutral pion decays:

1. Reconstruction efficiency must be optimized for benchmark decays to *all* final states. Many of these, such as $B^0 \to J/\psi K^{*0}(K^{*0} \to K_S^0\pi^0)$, $B^0 \to \pi^0\pi^0$ and $B^0 \to \rho\pi$ contain π^0's, where efficiency is rather low.

2. Combinatorial backgrounds, for analyses involving the reconstruction of π^0's from calorimeter cluster pairs, are generally high. These parts of the reconstruction are found to be the most unreliable.

3. Typical π^0 momenta in physics simulations are ≤ 1 GeV.

4. The di-neutral decay modes of the π^0 and η can be conveniently utilised to calibrate the electromagnetic calorimeter, using iterative peak-shifting procedures.

2.3   Neutral Pion Decays

Because the strong force does not violate CP invariance, the QCD Lagrangian will be invariant under chiral transformations. These transformations normally mix the left and right-handed fermion fields amongst themselves independently, implying that the QCD Lagrangian would be invariant to an $SU(3)_L \otimes SU(3)_R$ symmetry. As the vacuum $|\theta >$ is not invariant under these transformations, and the resultant massless left and right-handed quarks with identical weak coupling are not observed, this global chiral symmetry must be dynamically broken.

In a manner analogous to the famous Higgs mechanism, three broken chiral symmetry generators will result in three "massless" pseudoscalar Goldstone bosons. Comparing the negligible u and d quark masses and their almost unbroken symmetry, these Goldstone bosons can gain small masses ≈ 140 MeV, and are the isotriplet of light pseudoscalar mesons $\pi^\pm$, π^0. Consequently, the π^0 is the lightest pseudoscalar meson with a mass $= 134.98$ MeV, and is a bound state consisting of a quark and an anti-quark,

$$|\pi^0 >= \frac{1}{\sqrt{2}}|\bar{u}u - \bar{d}d > . \tag{2.21}$$

The dominant decay mode occurs via an electromagnetic process $\pi^0 \rightarrow \gamma\gamma$, which has a mean life $\tau_{\pi^0} \sim 8.4 \times 10^{-17}s$. With a large relativistic boost, colliders such as the Tevatron at Fermilab have the opportunity to study the $\pi^0 \rightarrow \gamma\gamma$ decay, using high resolution silicon vertex detectors. At $BaBar$, the photons are considered to originate directly from the interaction point. A calibrated EMC detector would

in this case be adequate to perform accurate measurements of the π^0 mass. The calculated width is reasonably small,

$$\Gamma(\pi^0 \to 2\gamma) = 4\pi\alpha^2 \ |f_{\pi^0}|^2 \ \frac{m_{\pi^0}^3}{16} \tag{2.22}$$

$$= 7.64 \ eV$$

and is in good agreement with experiment[8]. The decay process (Figure 2.3) is depicted by an isotriplet axial-vector current, coupling via a triangular fermion loop to two gauge bosons. Here, I_3 is the third-component of the isospin projection operator and $f_{\pi^0} \sim 9.3$ MeV is a constant related to the pion structure function, which characterizes our ignorance of the pion structure.
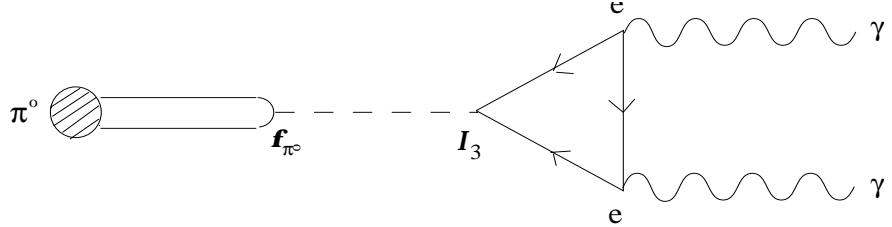
Figure 2.3: Diagram for the decay $\pi^0 \to \gamma\gamma$

2.3.1 The $\gamma\gamma$ Invariant Mass Equation

To determine the energy peak-shift of radiatively decaying mesons e.g. $\pi^0 \to \gamma\gamma$, $\eta \to \gamma\gamma$ for the detector calibration method, the invariant mass, m_{ij} must be calculated. This can be done by finding m_{ij} for all possible cluster pair combinations, using the measured energies E_i, E_j and the opening space-angle η

$$m_{ij} = [2E_iE_j(1 - \cos\eta)]^{\frac{1}{2}} \tag{2.23}$$

where m_{ij} is the equation for the invariant mass of two photons. This equation is derivable from the decay of the π^0 to two photons in it's centre-of-mass (figure 2.4). Using the conservation of energy and momentum, one finds

$$m_{\gamma\gamma}^2 = (E_1 + E_2)^2 - (\vec{p_1} + \vec{p_2})^2 \qquad (2.24)$$

$$\Rightarrow m_{\pi^0}^2 = 2E_1 E_2 (1 - \cos \eta) \qquad (2.25)$$

$$m_{\pi^0} = [2E_1 E_2 (1 - \cos \eta)]^{\frac{1}{2}}. \qquad (2.26)$$

It will be recognised later that equation 2.25 forms the basis of the π^0 invariant mass energy calibration procedure.
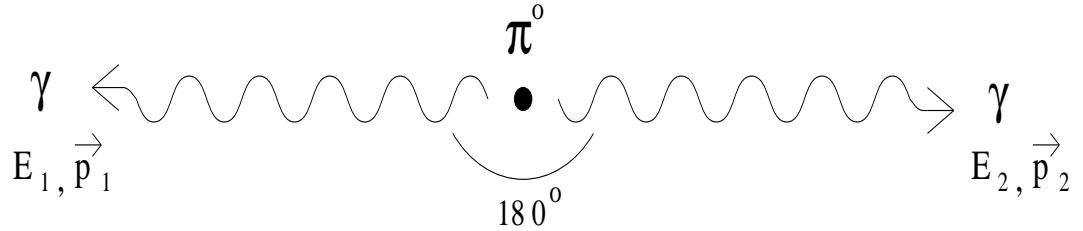
Figure 2.4: The decay of the π^0

Chapter 3

The Electromagnetic Calorimeter

3.1   The Electromagnetic Calorimeter

The prospect of observing CP violation in the B system has enforced major advances in both detector and accelerator technology. At PEP-II, (Figure 3.1) the aymmetric collisions of 9.0 GeV electrons with 3.1 GeV positrons are expected to produce a $\beta\gamma = 0.56$. A boost of that kind in the centre-of-mass frame in the laboratory will provide a ten-fold increase in the decay length of B mesons, a notable enhancement over existing symmetric storage rings. This will enable current silicon vertex tracking technology to resolve the time-difference between decay tags and CP eigenstates. If CP asymmetries were to be measured for the rapid frequency mixing of the B_s^0 - $\bar{B}_s^0$ system, then the predicted large value of the mixing parameter, x_s could only be studied experimentally at centre-of-mass energies above the $\Upsilon(4s)$ mass.[1] A design luminosity of $3 \times 10^{33} cm^{-2} s^{-1}$ will produce of the order of 2.5×10^6 $B^+ B^-$ and 2.5×10^6 $B^0 \bar{B}^0$ pairs per year, from the decays of the $\Upsilon(4s)$ resonance. This can be achieved by the generation of 1658 bunches, containing 2.73×10^{10} e^- and 5.91×10^{10} e^+ per bunch, at a 4.2ns beam crossing rate. High beam currents

---

[1] Currently there are no plans to do this with *BaBar*

of 0.99A and 2.14A will be accelerated by an improved r.f. superconducting cavity system. The beams will be supported by an upgraded high-energy ring (HER) and a newly constructed low-energy ring (LER), the former storing the electrons and the latter storing the positrons.
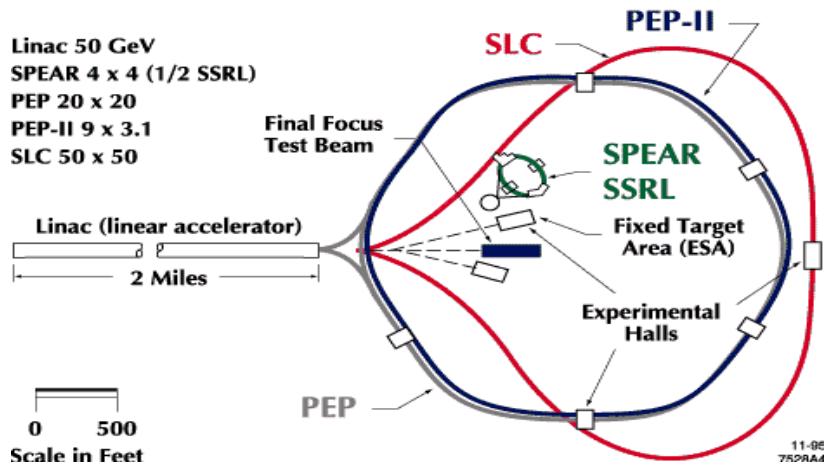
Figure 3.1: The PEP-II facility at SLAC

3.2   The Interaction Region

The Stanford B Factory, comprising the *BaBar* detector and the PEP-II storage rings, will be the first establishment as such in a burgeoning 'B Industry'. A host of other proposed experiments, including Belle, LHC B, HERA B, B-Tevatron and a CLEO-III upgrade will complement the physics results in the near future.

In order to achieve its primary objectives, the *BaBar* experiment has necessitated new developments, in facing considerable technological challenges. Including

the "standard" requirements of precision tracking and vertexing, excellent calorimetry is required, alongside accurate particle identification. These specifications have resulted in the design of a multi-purpose detector, consisting of many separate components and encapsulating much of the solid angle around the interaction region, (Figure 3.2).
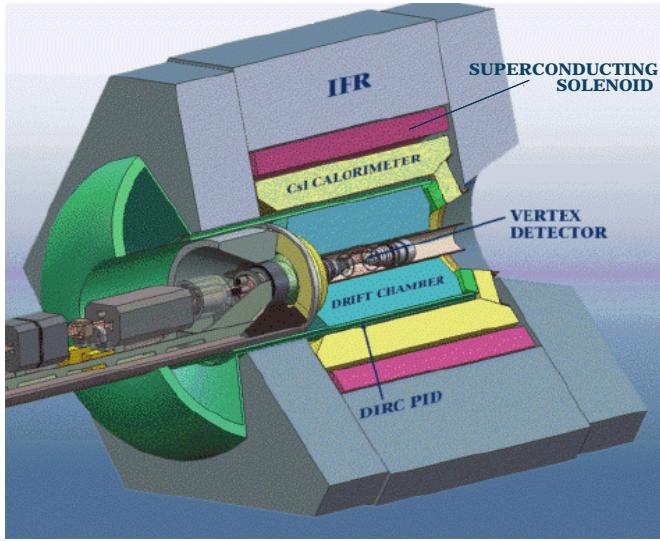
Figure 3.2: A schematic cut-away view of the *BaBar* detector

3.2.1 Detector Components

The *BaBar* detector will be comprised of the following components:

- A silicon vertex detector (SVT). Situated near to the beam-pipe, the silicon tracker consists of a five layered set of double-sided silicon microstrips, with a readout pitch of 100μm and 200μm in the inner and outer layers. This serves to measure accurately the spatial postion and directions of charged tracks. B vertices can also be separated with an intrinsic resolution of 12μm at normal

incidence, enabling increased background reduction capability and improved pattern recognition in rare B decay reconstructions.

- A Gas Drift Chamber (DC). This is composed of over 7000 wires strung axially in 40 cylindrical layers. Trajectories of charged particles can be tracked, and transverse momenta found from curvature measurements inside the axial magnetic field.

- A Detector for Internally Reflected Čerenkov photons (DIRC) will be used for particle identification, in particular kaon/pion separation. The ring imaging system passes totally internally reflected light along a quartz pathway, for detection by a series of photomultiplier tubes.

- An Electromagnetic Calorimeter (EMC) which consists of a cylindrical barrel section, (mounted asymmetrically about the interaction point) and a conically-shaped forward endcap. Employing 6580 thallium doped caesium iodide crystals, photodiode pulse heights allow the total energy deposition in the crystals to be determined. The calorimeter must satisfy an energy measurement precision of approximately 1% at 1 GeV, whilst covering a photon energy range from 20 MeV up to 4.1 GeV. This allows a neutral pion mass resolution of 7 MeV. As a result the calibration and monitoring procedures will provide special challenges.

- A Superconducting Solenoid entailing a 3m diameter, 3.75m long cryogenically-cooled magnet, providing a homogeneous axial field of 1.5 T, to aid the momentum measurement of charged particles.

- An Instrumented Flux Return (IFR). The IFR provides an iron return yoke for the solenoidal field. It is comprised of 20 iron plates, interspersed with Resistive Plate Chambers. The instrumentation supplements the EMC in the identification of muons, which penetrate the rest of the detector.

3.3 Calorimeter Overview

3.3.1 Calorimetry Requirements

The *BaBar* EMC has been designed and constructed to meet specific performance criteria. Reconstructing *CP* eigenstates containing one or more π^0's requires a calorimeter with high efficiency, to counter the small branching fractions expected. The high efficiency needed will be catered for by the minimization of material preceeding the calorimeter (material in front of the calorimeter does not affect resolution), and in the use of low noise preamplifiers and digitising electronics for the DAQ and crystal readout system. The calorimeter must also be sensitive to low energy photons if final state π^0's, which are produced copiously in B decays, are to be detected efficiently. Good energy and angular resolution is also needed to improve the π^0 and B mass resolutions, leading to increased signal-to-background ratios for rare decays. The fine granularity of the calorimeter, and improvements in crystal growing methods should ensure that an energy resolution for the crystals of

$$\frac{\sigma(E)}{E} \approx \frac{1.0\%}{\sqrt[4]{E}} \oplus 1.2\% \tag{3.1}$$

will allow these criteria to be fulfilled.

Another essential requirement which the calorimeter must satisfy involves electron identification, where e/μ and e/π separation can provide useful tags for subsequent analyses.

3.3.2 Description of the Calorimeter

The EMC is comprised of a cylindrical barrel section (mounted asymmetrically about the interaction point), and a conical forward endcap. A total of 6580 caesium iodide crystals are arranged in a quasi-projective geometry inside the calorimeter, with each crystal varying in radiation length X_0 and orientated to face toward

the interaction point. The barrel section contains 5760 of the crystals, arranged in 48 rows of distinct sizes, each having 120 identical crystals in azimuth. For the endcap, 820 crystals are confined to 20 separate modules, each having eight radial rows.

The support structure for the crystals must be rigid, and should introduce the minimum possible amount of material between crystal blocks and in front of them. This is achieved by utilising a modular scheme for the calorimeter construction, where each module is made from a thin honeycomb-like carbon-fibre composite structure. In the barrel, modules are suspended from a large aluminium cylinder, whilst the endcap is suspended from a large steel ring. (Figure 3.3 displays the crystal arrangements within the calorimeter).
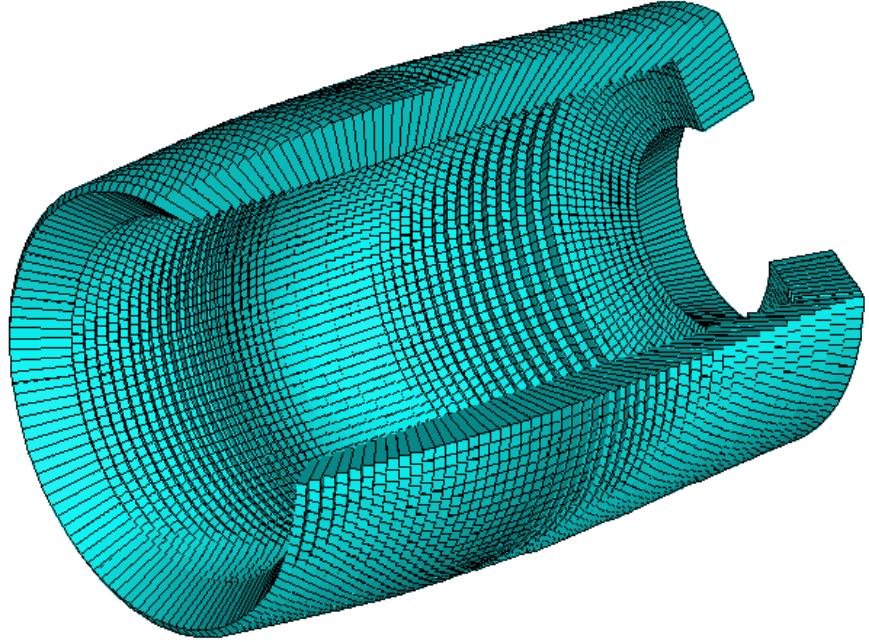
Figure 3.3: Crystal arrangements in the Electromagnetic Calorimeter

The endcap, which forms a plug at the forward end of the calorimeter covers a solid angle between $\cos\theta = 0.97$ and $\cos\theta = 0.89$ in the laboratory. It has been designed to split into two parts for installation around the beam-pipe, and

Properties	CsI(Tl)
Radiation Length (cm)	1.86
Absorption Length (cm)	34.2
Light Yield (Photons/MeVx10^3)	50-60
Light Yield Temperature Coef. (%/°C)	0.1
Moliére Radius (cm)	3.8
Peak Emission (nm)	565
Lower Wavelength Cutoff (nm)	320
Refractive Index at Emission Maximum	1.79
Decay Time (ns)	940
Density (g/cm^3)	4.51
Hygroscopic	slight

Table 3.1: CsI(Tl) crystal properties

must match the conical cross-section of the barrel with a minimum of deadspace. To achieve near hermiticity around the interaction region, the clearance between individual modules is only 0.5mm, and the difference between the conical surfaces of the endcap and barrel are of the order of 2mm. The individual crystals are tapered and are trapezoidal in shape, and have a typical length of 30cm (lengths vary from 16 to 17.5 in radiation length, X_0),[2] with front and back face areas of $4.75cm^2$ and $6.05cm^2$ respectively.

3.3.3 Calorimeter Interactions

Caesium iodide was chosen as a material for the calorimeter, as it is a proven technology and has well defined scintillation light yield properties (Table 3.1). The charged and neutral particles which interact with the CsI produce photons, electrons and positrons in a variety of physical ways. The processes that take place involve Bremsstrahlung and pair-production for electron/photon electromagnetic

---

[2]One radiation length is defined as the distance over which an electron loses 1/e of its energy via bremsstrahlung radiation. The radiation length is dependent upon the Z and A values of the medium

interactions, and secondary π^0 and hence electromagnetic shower production, via the strong interaction of charged pions[9]. Charged pions also lose energy by dE/dx loss continuously throughout the crystal. As in most calorimeters, the number of particles produced in a shower increases with the energy of the incident particle, and the depth of a shower varies as the logarithm of the initial particle energy. A shower will contain a maximum number of particles N_{max} at the critical energy E_c, where the ionization loss is equal to the particle's energy:

$$N_{max} = \frac{E_0}{E_c},\qquad(3.2)$$

the number of particles is therefore proportional to the incident energy, E_0. The mean energy deposition for an electromagnetic shower can be used to calculate analytically the depth at which a shower may occur, as a function of energy [22]:

$$D = 5.45 + 0.97\ln(E[MeV])\qquad(3.3)$$

where D is the shower deposition depth in centimetres. Whereas the depth of an electromagnetic shower is quite well-defined, a strong interaction can occur anywhere in a crystal, with a distribution exponential in form, characterized by a strong interaction length. Photons with intermediate energy (such as those arising from π^0 decays) may therefore shower deep inside the calorimeter, leading to reductions in resolution due to energy losses. Shower non-containment is therefore a pricipal reason why energy scale calibration of the EMC detector is important.

Losses in energy can also arise from the "disappearance" of photons and other particles through gaps in the detector, such as those found between adjacent crystals. Energy losses such as these are a primary source of calorimeter resolution degradation. The effects are significant in π^0 reconstruction, where asymmetric Gaussian peaks are found to result,(Figure 3.4). The formation of 'low-side tails' are a notable feature of these mass resolution plots, which are caused by the folding together of two asymmetric photon lineshapes. Noise in the electronic readout system, the nature of the cluster-forming algorithms used, shower containment, transverse

energy losses, calorimeter granularity and crystal performance ultimately have a bearing upon this energy-shifting effect.
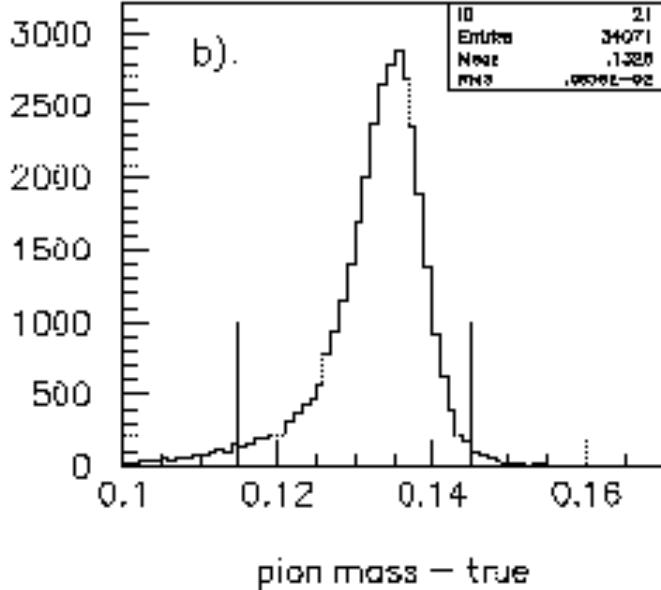
Figure 3.4: π^0 reconstruction detailing a shifted asymmetric peak

So, for a CsI(Tl) calorimeter and neutral pions with an incident energy of 1 GeV, the typical decay photons will produce a shower of $\sim$ 100 particles, at a depth of $\sim$ 10cm. A resultant shower of charged particles may also undergo multiple Coulomb scattering, for which much of the transverse spread in the shower development is contained within a circle of area πR_M^2, where R_M is defined as the Moliére radius, and is equal to the right hand side of equation (3.2)$\times X_0$, where $E_0 \approx 21$ MeV.

3.4 CsI(Tl) Crystals and Module Construction

Groups from UK universities and RAL are responsible for all aspects of the design, construction, installation, commissioning and operation of the EMC endcap. The *BaBar* group at Manchester is responsible for the construction of 10 of the 20

endcap modules. This work involved crystal quality control and quality assurance procedures, in ensuring that the crystals had the correct uniformity and light yield. Visual and dimensional inspections of each crystal were also undertaken, as precise tolerances ($\sim 150\mu m$) in the sizes were required for crystal module installation. Since the light output of a crystal should be uniform along the length of the crystal, great care has been taken to ensure that the crystals have been 'tuned' to produce a uniform light output. Crystal QC therefore involved scanning for light response uniformity along each crystal, using a collimated Na^{22} radioactive source under remote computer control. The light output was measured by a PMT at the base of the crystal. All data had to be within the required envelope, a deviation of not more than 2% from a standard reference crystal. Figures (3.5) and (3.7) show a typical CsI crystal and the cross section of a module-prepared crystal. Crystals which met

Figure 3.5: A CsI crystal

these specifications were wrapped in three insulating layers of Tyvek, Mylar and aluminium foil, to increase diffuse reflectivity and to provide r.f. shielding, ready for module insertion. They were then cabled for preamp electronics and fibre-optic calibration (figure 3.6), before final shipment to SLAC.

3.4.1   Handling Crystal Data

The development of a shower inside of an individual crystal is essentially a random phenomenon. Photons scattering in the trapezoidal geometry of a crystal renders the process as intrinsically non-uniform, so that the light output as a function of position along the crystal is non-linear. When a particle passes through the scintillating material of the crystals, photons are produced uniformly within a certain spectral range. For each crystal, these photons are collected by two independent Hamamatsu photodiodes which produce electrical signals. These signals are amplified by a pre-amplifying circuit, and are then inputted to ADC's which digitize the data for further analysis. Each of the 6580 crystals has its own trigger readout. For an event rate Φ, an instrument with dead time t can only measure a fraction f of the Poisson distribution of events:

$$f = \frac{1}{1 + \Phi t}.$$
(3.4)

During an experimental run, as the calorimeter trigger cannot handle all of the energy and time-of-deposition "feature extraction" information in the short timescale that events take place, smaller regions of crystals in 8 × 3 blocks or "towers", are summed in sectors of phi. Using this method, shower depositions overlapping many crystals are summed over quickly and efficiently, reducing the complexity of a potentially difficult problem. Maps are then produced to describe the total energy depostion in the calorimeter. The information can then be passed to the Global Trigger, which also receives information from the other components of the detector, for final decision making. In this way, calorimeter information corresponding to potentially interesting events can be processed 'in situ' as part of Online Event Processing (OEP), for further analysis.

3.4.2　Calorimeter Objects

All *simulated* crystal digitisations are stored as objects called hits, for manipulation by the EMC reconstruction software. These can be formed into further objects known as digis, clusters and bumps. A cluster is a continuously connected region of energy deposits in contiguous crystals, where each energy deposit has at least one neighbour, and one crystal has a deposition > 10 MeV. A bump is defined as a local maximum of a cluster. The position of a local maximum is equivalent to a bump's centroid, and the neighbouring crystals must have less than half of the bump's total energy. These objects comprise the 'raw' data which can be used for studies involving analysis, monitoring and calibration.
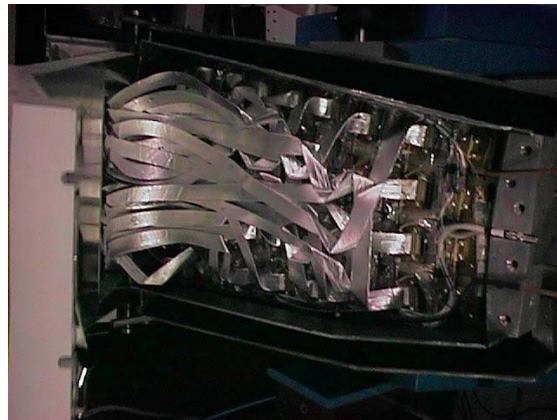
Figure 3.6: Module construction

3.5　Calibration and Performance Monitoring

Throughout the projected 10 year life of the *BaBar* experiment, less than one CsI(Tl) crystal and it's associated electronics readout and DAQ chain is required to fail. To attain this goal, a systematic programme of monitoring and calibration studies will be implemented during start-up, commisioning and throughout the duration of the experiment. It is anticipated that a large amount of time will be

spent in progressing through the calorimeter studies 'learning curve', in ensuring that progress can be made in the understanding and evaluation of the differences between the simulated studies, and the response and performance of the actual detector.

Considering the high radiation environment in which the crystals will have to operate, degradation in the performance of both the crystals and optical joints is to be expected because of radiation damage and ageing. Results from radiation tests on crystals have indicated that the loss of light is insufficient to degrade the energy resolution of the calorimeter. Changes in effective light yield and in the uniformity of the crystal response must still be monitored precisely, however, if the energy resolution is to be maintained.

At intermediate energies, the calorimeter is effectively self-calibrating, using physics processes involving photons. Although, the 'Calorimeter Calibration Task Force' [11] have argued that these are not always the simplest and fastest methods of keeping track of variations in response over the whole energy range. The task of monitoring crystal gain changes over short periods of time has been accounted for in the novel introduction of a light pulser system to the baseline design.

3.5.1 The Light Pulser Monitoring System

Monitoring is essentially a complementary procedure to calibration. The two processes may act in tandem. The changes in the response of the system can be monitored, and those changes can be used in the correction and compensation of those variations, in the determination of calibration constants (figure 3.8).

In between calibration runs, the relative performance of all of the crystals will be monitored continuously with a pulsed fibre-optic system. This consists of a number of Xenon flash lamps arranged such that light pulses are passed via fibre bundles and filters into the rear of each crystal (figure 3.9). The light pulser system

is designed to take data over a short timescale, enabling monitoring to take place continuously, with a precision of less than 0.1% on a pulse-to-pulse basis. In this way, the effects of gradual drifts in individual crystal constants can be elucidated, when the light-pulser system data is compared to other calibration and monitoring tools. Calibration constants derived from the π^0 invariant mass method will not be derived within a timescale fast enough to track crystal changes. This method may evaluate long-term gradual changes in the overall response of the calorimeter. A *fast* response to the changes in relative crystal constants is therefore possible with the pulser. The diagnosis of problems relating to the following effects of:

- radiation damage

- changes in uniformity and light yield from temperature and humidity fluctuations

- deterioration in the optical properties of joints

- photodiode adhesive crazing

- ion absorption

- wrapping reflectivity changes

will also be accessible.

3.5.2   Radioactive Source and Electronic Calibration

Because of the importance of very precise calibration at low energies, a technique involving the pumping of a short-lived liquid radioactive isotope, around the front faces of the crystals has been developed. The decays of the isotope ^{16}N to the excited state ^{16}O produces a source of 6.1 MeV photons, sufficient to secure the sensitivity to photons down to 20 MeV. The radioactive source calibration can

only be performed with no beam present, but may provide a calibration point with a precision better than 1% within 15 minutes.

Advances in crystal growing techniques, electronics development and mechanical design have enabled an overall improvement in the *BaBar* EMC, over earlier designs. Electronics calibration can be achieved by linearization of the response of the front-end electronics. A preset charge injection is used to derive corrections from a comparison with the peak ADC and pedestal sample, before filtering and scaling is performed, from source or Bhabha calibration data. The resultant corrected values are then stored for each ADC channel, as 16-bit integers in a lookup table. These crystal gain constants are then available for use in feature extraction, trigger energy summation, and for adjustments during reconstruction. In this way, incoherent noise in the electronics can be reduced to approximately 150 KeV for each crystal, during physics runs involving intermediate energies. Due to the ineffective nature of the π^0 photon calibration at energies lower than 20 MeV, the use of a radioactive source will be essential in determining crystal response at the low energy scale. Measurements taken at this scale will enhance reconstruction efficiency and provide invaluable low energy calibration data.

3.5.3   Colliding Beam Calibration Events

Absolute calibration using physics processes essentially involves the measurement of the behaviour of the system to particles of known energy, type and spatial position. Energy response to known stimuli like the above are used to provide a greater understanding of the physics significance of the event data, and to enable the detector to be optimized for subsequent data-taking. Calibration methods frequently employ fitting or iterative procedures, which allow the response of the detector to be used in the elucidation of crystal calibration constants. For simulated events, calibration constants provide data which can be analysed to determine

the effects of detector geometry on physics results. Both staggered and 'saw tooth' crystal arrangements, and extra material have been investigated. Corrections have then been derived for $\gamma\gamma$ events. High yield non-radiative Bhabha events (e^+e^- final states) are a good example of how clean physics events are used[12]. For a range in energies of 3.0 GeV up to 9.1 GeV, data-sets from direct $\Upsilon(4s)$ decays to e^+ and e^- are obtained. These can be utilised in the extrapolation of an appropriate calibration energy scale, and to aid in the interpretation of temporal gain changes. Other physics events including radiative Bhabhas, $\gamma\gamma\gamma$, various D-meson signals and of course, π^0 diphoton decays provide similar methods to the above. Each of these examples is used primarily to calibrate at intermediate energy scales. Moreover, the diverse nature of these events ensure that useful cross-checks and comparisons of the full detector response can be made.

Since the minimum accepted polar angle is 20^0, seven rings at the rear barrel can be calibrated only using single Bhabha positrons and electrons. Beyond this acceptance, shared electrons must be utilised. The innermost instrumented endcap ring cannot be calibrated at all, however, with Bhabhas or any other physics events. For this reason, and because of the high radiation environment expected, the innermost ring of crystals has been replaced with blocks of carbon fibre in the final constructed endcap.
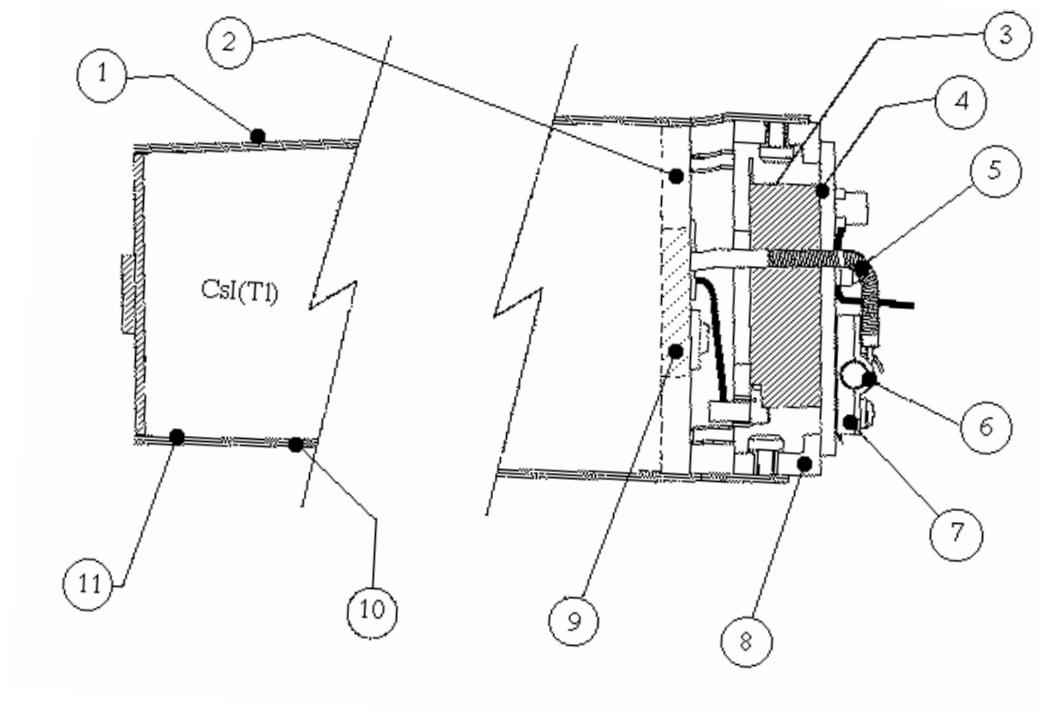
Figure 3.7: Cross section of a CsI(Tl) crystal: (1) Tyvek, (2) spreader plate, (3) metal enclosure for pre-amps, (4) brass backplate, (5) optic-fibre guide, (6) cooling pipe, (7) insulated pipe holder, (8) standoff, (9) PIN photodiode, (10) Al foil, (11) Mylar.
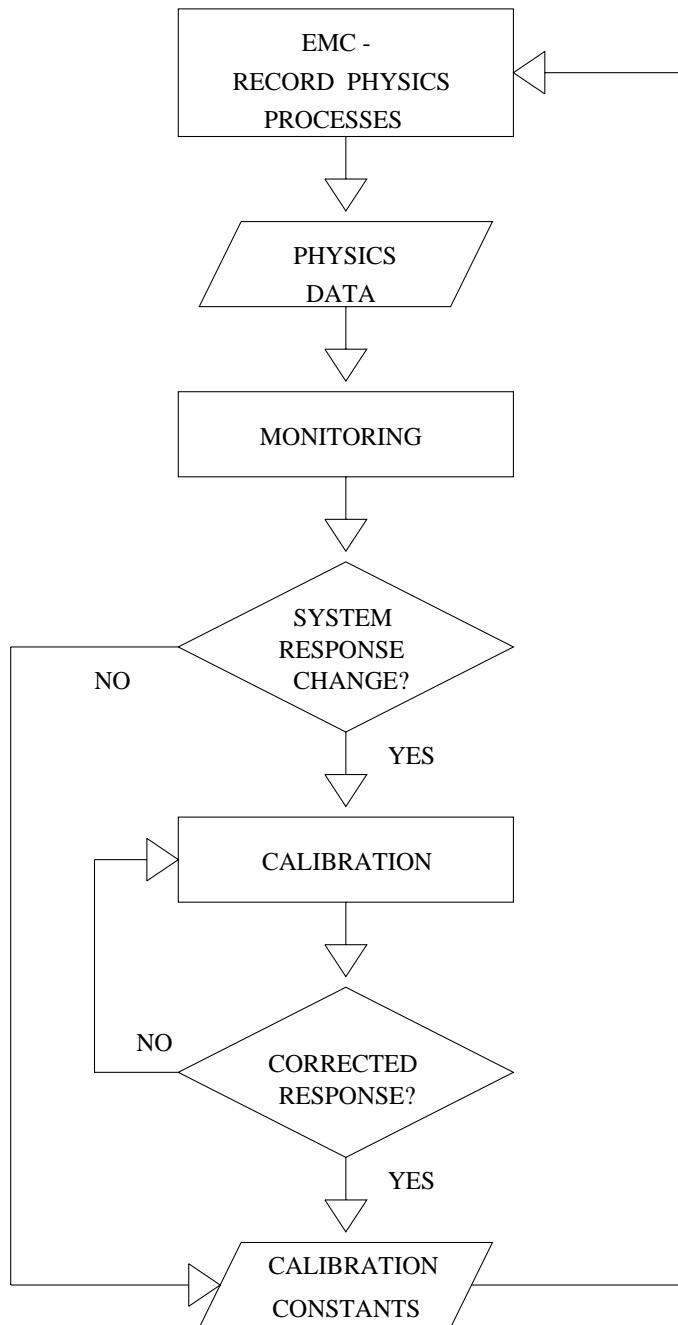
Figure 3.8: Calibration and monitoring EMC system flow chart
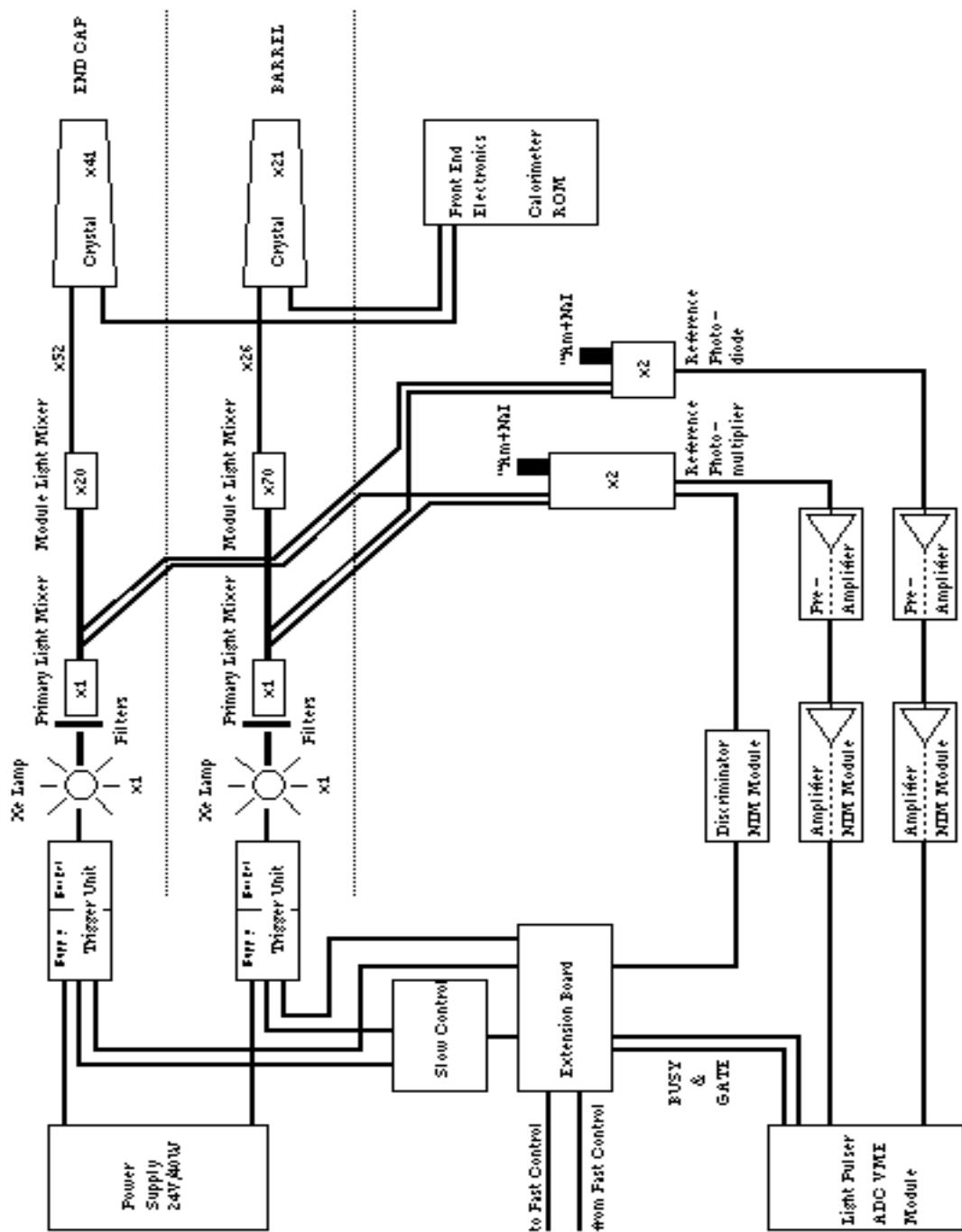
Figure 3.9: The Light Pulser System

Chapter 4

Software

4.1 Software

C++ is a highly versatile and robust industry standard programming language. It has many distinct advantages over problem-oriented languages such as FORTRAN, and is well suited for the development of large projects involving many users. The capability of using Object Oriented Design methodologies allows for greater flexibility over previous languages, including ease of code re-use, which increases efficiency and shortens code development time. C++ was initially developed as a superset of the C programming language called C with classes, by Bjarne Stroustrup at AT & T Bell Laboratories in 1985 [13]. The name C++, or 'the incrementation of C by one unit' aptly implies an evolution in C, which has a similar syntax.

4.1.1 The BaBar Framework and OOP

The power of the Object Oriented Programming (OOP) style supported by C++, was instrumental in the decision to adopt it as the preferred language for

BaBar. The experiment will be the first in High Energy Physics to use C++ at the data acquisition, reconstruction and analysis stages. Object Oriented Programming advocates three methods of structuring programs:

- procedural programming

- data abstraction

- modular programming

Procedural programming involves logical procedures, and the implementation of the best algorithms to perform required tasks. Data abstraction methods are based upon the provision of user-defined types and a full set of operations for each type (i.e defining complex numbers and finding their moduli). Modular programming places emphasis on data organisation and related procedures, which are grouped into modules. The latter style is predominantly used in the *BaBar* Framework, of which the basic unit is the module. A module contains code which takes various data from events, runs specific algorithms, and returns results for later analysis.

The module used to perform photon energy calibration using π^0 decays functions in exactly the same way. Initial calibration constants are extracted from a file, and are used with all measured photon energy values from events to find the true position and minimum width of the invariant $\gamma\gamma$ mass peak. Algorithms that find and shift the peak using iterative procedures are then employed, alongside many more that perform tasks such as spline interpolation, neutral cluster isolation and background fitting. Finally, the minimization of the likelihood function of the calibration procedure results in the output of analysed histograms and a file of derived correction coefficients for every energy bin of photons. The calibration module is described in greater detail below.

One of the main features of C++ is the class, an idea borrowed from the earlier Simula 67 language. A class is similar to a structure in C. The creation of

a class, with appropriate member functions and data members enables objects to be defined such as clusters and bumps, which are variables of user-defined type. The framework consists of a set of such classes, that provide a structured interface between code which performs different tasks and allows for code re-use between subsystems through inheritance. Examples of tasks which are provided by the framework package are calibration, input and output of events and management of the event processing loop. Knowledge of the arcania of C++ is therefore kept to a minimum for users, since specific solutions are already provided for coding environments such as reconstruction, OEP and analysis.

4.1.2 *BaBar* Computer Simulation

Extensive studies have been performed using computer simulations of the *BaBar* detector performance, in reducing background and measuring physics channels of interest. These have been carried out using two different simulation packages, ASLUND and BBSIM. The former is a fast Monte Carlo, while the latter is a detailed simulation based upon the GEANT package developed at CERN. ASLUND consists of two main components, an event generator and a parametric simulation of the detector to provide particle calorimetry, particle identification and charged tracking.

The package BBSIM was used extensively throughout this investigation of background reduction in the energy calibration procedure. It comprises a description of the detector geometry and the capacity for full simulation of the range of interactions expected within the detector. Detector response and subsequent analysis are studied using generated events, which are stepped through the simulated detector. In determining EMC calibration response to photons of varying angle and energy, neutral and charged particles are interacted with a subpackage representing the calorimeter. Positions and depositions within the barrel and endcap, which are

modelled as a non-segmented cylinder of caesium iodide, are registered as hits in individual crystals or blocks. In the real detector, these interactions will be registered as digitised signals from the crystal readouts, called digits.

All possible physics events of interest have been simulated and stored as 'mock data' files on tape for ease of analysis. These files are known as BEAST (*BaBar* Event Analysis Summary tapes). They are produced when BBSIM outputs files to the BEAR software package. These tapes will eventually be replaced with a repository to store the data from real events.

4.1.3 Reconstructed Data

Data from the simulation is used to reconstruct physics events. The input to EMC reconstruction consists of a list of crystals, with each single crystal having an energy above a threshold of 0.5 MeV. The energy in a given crystal is processed online. This means that individual crystal calibration constants (from for example, Bhabha colliding beam calibration events) are applied during online event processing. Crystal geometry data, charged track, IFR, DIRC and event vertex information are additional data needed to fully reconstruct events.

The EMC reconstruction uses geometry files to reconstruct digis from hits, clusters from digis, bumps from clusters and other related objects. A shower energy calibration is available in reconstruction based on Monte Carlo studies. Since crystal shower calibration constants are already applied during reconstruction, the module `EmcCalPi0` has been implemented using "unreconstructed data"[1]. The package EmcReco contains some classes which provide clustering and bump finding algorithms in a manner similar to the above. However, no energy calibration corrections are applied at this stage.

---

[1] The term "unreconstructed data" will be used to describe the data which does not include this shower energy calibration, but which does include single crystal calibrations.

To observe the effects of these calibration corrections, the package `BetaUser` was used to reconstruct π^0 decays to two gammas. This was originally done using the release 5.3.2, a corrected and updated beta version of earlier releases. The acquisition of reconstructed data from the tape storage silo onto a tape suitable for reconstruction running, or 'staging' had to be done before any compiling or linking of the code could take place. The .tcl module control script, which activates certain modules and also subdetector components in the package, was used to provide a pointer to a file, electrons.xdr. This contained a link to the original file staged to disk. The file contained $\pi^0 \rightarrow \gamma\gamma$ decays with π^0 momenta in the range $5.0 > p > 0.5$ GeV, of the Mock Data Challenge set of events. After the correct tape had been staged, the module, including the file `MySampleBetaAnalysis` was compiled and linked ready for running.

`MySampleBetaAnalysis` is a prototype file that users can modify in order to do their own analysis. Figure (4.1) shows the di-neutral spectrum for $\Upsilon(4s) \rightarrow B^0\bar{B}^0 \rightarrow Q\bar{Q}$ + background events. These histograms indicate the presence of a large background, caused by the neutral cluster-merging algorithm used in the `BetaUser` analysis. An invariant mass peak close to that of the π^0 can be seen for the Monte Carlo di-neutral match, which takes the Monte Carlo truth energies of neutral clusters and bumps, and forms neutral candidates from all pairs. Combinatorial background due to the presence of noise and wrongly combined pairs can be seen below the small peak. No peak was distinctly observed for the compared di-neutral spectrum. For the histogram of figure (4.2), only di-neutral combinations were selected. The cuts placed were $0.11 < m_{\gamma\gamma} < 0.15$ GeV. This histogram of the total number of entries versus the invariant mass of the two gammas clearly shows an invariant mass peak which is close to the π^0 invariant mass. This was formed by combining neutral clusters over all energies. Better cuts would increase the efficiency (table 4.1) and would help to eliminate the observed background, resulting in a well defined peak.

The next step taken was to determine the number of clusters and bumps, which are split clusters, formed at differing energies. This would enable one to determine the number of individual clusters and bumps expected at certain energies, and could prove useful in rejecting clusters and bumps that constitute background. These should not be included in the iteration over neutral candidates. First, a pointer to a function which accessed an array of objects as cluster energies was included in the code. These cluster energies were then looped over for 100 events and finally binned for the number of single and paired clusters formed over the energy interval 1.0 to 5.0 GeV. The resulting cluster energies were appended to a log, and are shown in table (4.2).

It can be seen that the number of clusters formed by the two dimensional clustering algorithm decreases with increasing energy. This could be explained by the behaviour of the clustering algorithm, or because there may really have been fewer clusters to begin with.

The way in which clusters are formed from individual hits in the calorimeter involves a summing of crystal blocks, with the total number of blocks being summed varying as a logarithmic function of energy. Of the order of 4 blocks are summed at an energy of 25 MeV, rising to 17 blocks for energies of the order of several GeV. A cluster in this context is defined as that region in which the total energy deposition > 10 MeV. Summing over contiguous neighbours, which must not be isolated by more than two blocks from the main deposition, can then give the position of highest energy deposition. The relative positions of clusters are then adjusted from the centroid using a weighted mean and crystal penetration depths and lateral adjustments calculated. This feature of the clustering algorithms has particular importance for the angular resolution of clusters found in the endcap.

Histograms of the total number of bumps and clusters were then produced for 2×10^3 events (figure 4.3). The number of bumps and clusters produced were found to increase with energy to a maximum, and decrease accordingly. At higher

energies, ~ 400 pairs of clusters were seen. The total number of entries where no clusters were found was about 200. Again, with energy increasing to the right of the histograms, 200 entries with no bumps were found. Over 900 single bumps and under 1000 bump pairs can also be seen.

These effects can be accounted for if the merging of clusters (at higher energies) is considered. At higher energies, the number of cluster pairs found is lower than the number of single clusters. These single clusters have an increased probability of being separated to form bumps. With increasing energy and greater shower production, paired bumps are at a maximum. More bump pairs than singles can be seen, because both decay photons are individually resolved as bumps, or localised energy deposition maxima, at higher energies. Above 3 GeV, these photons are from π^0 decays. Single bumps may correspond either to blocks that contain two unresolved photons, or to photons that have to be combined into pairs.

The exercise in manipulating reconstructed data and in using the package `BetaUser` provided familiarity with the framework, and served to clarify further the nature and action of the cluster-forming algorithms. However, to fully investigate the energy calibration procedure it was necessary to use the "unreconstructed data". The module `EmcCalPi0` has been implemented with the class `EmcMakeABsCalPi0` and can be used for such a task, with useful classes available from the module `EmcReco`.

4.2   The Calibration Module

From the equation for the invariant mass of two photons (2.25), the uncalibrated γ energy has the following relationship

$$\zeta = f(E, \theta)E \qquad (4.1)$$

which enables the observed photon cluster energy depositions to be corrected, using a searched for calibration function. The calibration function

$$\frac{\zeta}{m_{\pi^0}} = f(E, \theta) \tag{4.2}$$

has the explicit form

$$f(E, \theta) = \exp(A_1 + A_2 \ln E + A_3 \ln^2 E + A_4 \cos\theta + A_5 \cos^2\theta + \ldots + A_n). \tag{4.3}$$

To illustrate how the calibration function may correct the measured invariant mass, consider a correction factor equivalent to $f(E, \theta)$:

$$\frac{\zeta}{\Omega} = m_{\pi^0} \tag{4.4}$$

$$\frac{270 MeV}{2.0} = m_{\pi^0} \tag{4.5}$$

where ζ is the uncorrected γ energy, Ω is the correction factor and m_{π^0} represents the corrected γ energy. For example, in equation (4.5) if the observed photon energy deposition is 270 MeV, then a correction factor of 2.0 is clearly needed in order to calibrate the uncorrected energy ζ to the corrected π^0 mass. The calibration function is effectively used to fit an asymmetric lineshape or trendline to the peak. It is a polynomial function, logarithmic in powers of energy and theta angle to order n.

4.2.1   The Calibration Method

The initial set of A_i are called the distortion coefficients; values for these are estimated before the procedure of peak iteration and adjustment takes place. After succesive iterations, the A_i [2] become correction coefficients. These are saved to a separate file `EmcCalPi0.const` and are used for the next peak iteration. Calibration takes place through the minimisation of the likelihood function (4.6). When this

---

[2] Where the subscript i are integers, $A_i = A_1, A_2, A_3, A_4 \ldots$

has been achieved, the true position and width of the π^0 mass peak can be found. The likelihood function for the calibration procedure can be written in the following form, where $m_{inv,j}$[3] is equivalent to $m_{\pi^0}^2$ in equation (2.25) and m_0 is equivalent to $m_{\gamma\gamma}$, the mass of the $\gamma\gamma$ peak:

$$\mathcal{L} = \sum_{j=1}^{N} 2 \left(\frac{1}{2} \ln m_{inv,j}^2 - \ln m_0 \right)^2 \tag{4.6}$$

The first auxilliary variable becomes equation (4.7). Proceeding in this way, auxilliary variables can be defined (equations 4.8, 4.9 and 4.10) for the elements of the minimization matrix (4.18).

$$\lambda_{1j} = 1 \tag{4.7}$$

$$\lambda_{2j} = \frac{1}{2}(\ln E_{1j} + \ln E_{2j}), \quad \lambda_{3j} = \frac{1}{2}(\ln^2 E_{1j} + \ln^2 E_{2j}), \tag{4.8}$$

$$\lambda_{4j} = \frac{1}{2}(\cos \theta_{1j} + \cos \theta_{2j}), \quad \lambda_{5j} = \frac{1}{2}(\cos^2 \theta_{1j} + \cos^2 \theta_{2j}) \dots \tag{4.9}$$

$$\rho_j = \ln \left[\frac{m_0}{\sqrt{2\zeta_{1j}\zeta_{2j}(1 - \cos \eta_j)}} \right] \tag{4.10}$$

For the above auxiliary variables, the terms inside brackets correspond to observables, as measured by the electromagnetic calorimeter. In the `EmcCalPiO` calibration module, algorithms are used to return confidence levels for an observation to be consistent with a given particle hypothesis. In this case, the observables correspond to the energy depositions and angles for each pair of photon clusters when all blocks are iterated over by the clustering algorithms. This method allows each cluster to be paired and combined with all of the other clusters. The invariant $\gamma\gamma$ energies are binned by energy, for the number of entries produced. Interpolating the photon lineshape for individual energy bins with splines is also more manageable, as the peak has been divided.

Each observation gets manipulated as a list of objects in an array. C++ operations defined on these objects can then be used to find the most probable

---

[3]The index j labels the j-th pair of the photons' clusters

peak position, the position of the first filled energy bin and the maximum of the peak, for example. The code has been structured such that incrementation, operator overloading and matrix operations (as defined in the CLHEP class library of useful HEP classes) are facilitated to perform these tasks accurately and efficiently. The auxilliary observables are defined as follows:

- E_{1j} is the energy deposition of the first cluster for the jth pair of the photon clusters.

- E_{2j} is the energy deposition of the second cluster for the jth pair of the photon clusters.

- η_j corresponds to the space angle between both clusters in the jth pair.

- θ_{1j} and θ_{2j} are the θ angles of these clusters.

Using equation (4.1), the partial derivative of ζ with respect to A_1 is

$$\frac{\partial \zeta}{\partial A_1} = \frac{\partial f(E,\theta)}{\partial A_1} E = f(E,\theta)E = \zeta, \tag{4.11}$$

and the partial derivative of $m_{inv,j}^2$ with respect to A_1 is also

$$\frac{\partial m_{inv,j}^2}{\partial A_1} = 2\left(\frac{\partial \zeta_{1j}}{\partial A_1}\zeta_{2j} + \zeta_{1j}\frac{\partial \zeta_{2j}}{\partial A_1}\right) \times (1 - \cos \eta_j) \tag{4.12}$$

$$= 2(\zeta_{1j}\zeta_{2j} + \zeta_{1j}\zeta_{2j})(1 - \cos \eta_j). \tag{4.13}$$

Partially differentiating the likelihood function $\mathcal{L}$, with respect to A_1 gives

$$\frac{\partial \mathcal{L}}{\partial A_1} = \sum_{j=1}^{N} 2\left(\frac{1}{2}\ln m_{inv,j}^2 - \ln m_0\right)^2 \frac{1}{2m_{inv,j}^2}\frac{\partial m_{inv,j}^2}{\partial A_1}. \tag{4.14}$$

The maximum likelihood estimate says that this gradient is zero

$$\frac{\partial \mathcal{L}}{\partial A_1} = \sum_{j=1}^{N} 2\left(\frac{1}{2}\ln m_{inv,j}^2 - \ln m_0\right)\frac{1 \times m_{inv,j}^2}{m_{inv,j}^2} = 0 \tag{4.15}$$

Using the auxilliary variables and equations (4.16 and 4.17) the maximum of the peak and its width for each succesive peak iteration, using all photon clusters

are calculated. Some typical values after one calibrative iteration for the minimised likelihood are given in table (4.3).

$$\mathcal{L}\lambda_{kj} = 0 \tag{4.16}$$

$$\sum_{j=1}^{N} \left(\frac{1}{2} \ln m^2_{inv,j} - \ln m_0 \right) \lambda_{kj} = 0 \tag{4.17}$$

Although the re-positioning of the peak is usually precise, the width was frequently not optimized to be at its narrowest. As a result, the likelihood values were only found to equal zero on a small number of occasions, within small errors. In minimising the Likelihood function, one has to solve the symmetric matrix of linear equations for the searched coefficients, A_i:

$$\begin{pmatrix} G_{1,1} & G_{1,2} & G_{1,3} & G_{1,4} & G_{1,5} & \dots & \bigg\| & R_1 \\ G_{2,1} & G_{2,2} & G_{2,3} & G_{2,4} & G_{2,5} & \dots & \bigg\| & R_2 \\ & \vdots & & \vdots & & \dots & \bigg\| & \vdots \\ G_{5,1} & G_{5,2} & G_{5,3} & G_{5,4} & G_{5,5} & \dots & \bigg\| & R_5 \\ & \dots & & \dots & & \ddots & \bigg\| & \vdots \end{pmatrix} \tag{4.18}$$

such that the R_k have zero as the values of their solutions

$$R_k = \sum_{j=1}^{N} \lambda_{kj} \times \rho_j = 0 \quad \forall \quad k \tag{4.19}$$

This is done by diagonalizing for the gradients G, given by

$$G = \frac{\partial R_k}{\partial A_l} = \sum_{j=1}^{N} \lambda_{lj} \times \lambda_{kj} \tag{4.20}$$

where

$$\frac{\partial \rho_j}{\partial A_l} = \lambda_{lj}. \tag{4.21}$$

The procedure involves the following steps:

1. Initial values for the A_i are estimated.

2. The R_k, using the auxilliary variables and other relations given above are then calculated. If their values are all equal to zero to within errors, then the

function has been correctly minimized. If the R_k are not all equal to zero, then the gradient, G must be calculated. To do this, the A_i are perturbed by a small amount $A_i \rightarrow A_i + \delta$ during iteration.

R then becomes:

$$R \rightarrow R + \left(\frac{\partial R_k}{\partial A_l}\right)\delta_l. \qquad (4.22)$$

For the R_k to again equal zero then $R + G\delta = 0$, because $\delta = -G^{-1}R$ and $R = -G\delta$. If $R_k \neq 0$ at any particular step, then this procedure is repeated continuously until *all* of the $R_k = 0$. The resultant perturbed values of the A_i are then used to calculate the new R_k, proceeding again from step one.

4.2.2 Iterating the $\gamma\gamma$ Mass Peak

Iteration involves a method by which an initial estimation is given for a value, which may be inaccurate to start off with. Better and better approximations are then computed until the solution is converged upon with the desired accuracy. The quality of the iteration method can be specified by the speed of its convergence. Typically, the π^0 peak has to be iterated 5 or 6 times before acceptable peak positions are found. Figure (4.4) shows the results of the iteration procedure after some iterations. It can be seen that the uncalibrated peak position (solid line) has been shifted further to the right (dotted line) after calibration, *closer* to the correct invariant mass point. The machinery described in the previous section has been used to 'pull' the $\gamma\gamma$ mass peak closer towards to the proper place. As will be described later, CLEO-II do not shift to 135 MeV because this overshifts the gamma energy peaks (due to the asymmetric tails). CLEO-II aim to get the mass peak in the wrong place but by the right amount. Conversely, *BaBar* are aiming to get the mass peak in the right place by the 'correct amount', but instead are gaining an 'incorrect amount'. Some of the code implemented to do this contains standard procedures, which have been written previously in FORTRAN for the CLEO-II ex-

periment. Essentially, the basic premise of the entire calibration procedure rests upon the fact that the energy input does not equal the energy output. Iterating the invariant mass histogram peak back to 135 MeV remedies the problem because

$$\ln \left| \frac{m_{\gamma\gamma}}{m_{\pi^0}^{inv.}} \right| \rightarrow 0 \qquad (4.23)$$

is set as close to zero as possible. A fit to the photon lineshape given by the coefficients of the correction function must be varied until they approximate the expected, rather than the measured lineshape. Because the formula for the correction function will only give exact numerical solutions in all but the simplest of cases, (when many of the coefficients are zero) then the approximation method of iteration must be used. The Gaussian fit to the once iterated peak of figure (4.5) which agrees to within 5.5 % of the proper invariant mass value, did not match the asymmetric, skewed peak well. In the `EmcCalPi0` module code, a better calibration fit is performed when the best fit is found, using the member function `EmcMakeABsCAlPiO::fitPoly3()` and the peak parameters. Protected member function `EmcMakeABsCalPiO ::BestPeak` loops over all possible peak positions and includes the searched-for minimum likelihood values; it takes as its arguments the parameters:

int Nbin number of energy bins in the histogram

double Hbin bin size

ksi1 centre co-ordinate of the first bin in the histogram

nP width of the peak region in bins

nHist array of histogram accumulators for the bins

The peak itself is shifted using the member function `PeakShift()`. This takes similar arguments and also returns the values of 0 or 1, for peak parameter-finding success or failure, after the relevant operations have been executed.

4.2.3 Spline Interpolation

Other member functions are supplied in the class `EmcABsCalPiO::smooth()`, which includes the spline interpolation procedure for the correction coefficients. Correction coefficients are obtained with greater accuracy if a good fit to the lineshape can be obtained. Spline interpolation, or sectionalised polynomial interpolation involves the dividing of the lineshape into separate bins. If the lineshape for the peak is considered to be a continuous function f (x), then this can similarly be divided into subintervals with common endpoints called nodes[14]. If these partitions are then regarded to consist of polynomials, then the function f (x) can be approximated even for polynomials of high degree n, by the subinterval functions g (x).

Therefore, f (x) is not approximated by a single polynomial over the entire interval, but instead by n polynomials. This method is generally more stable, and does not exhibit oscillatory behaviour as much between nodes. The reason for this increased quality of interpolation is due to the presence of continuous first and second derivatives everywhere in the intervals. Quadratic interpolation splines, where each polynomial partition has a degree of not greater than 2, have been used for several grouped terms of the correction function, for both the peak and the background intermediate regions.

4.2.4 Simplex Minimization

A simplex is an object in n dimensions, consisting of the lines that connect $n + 1$ points. For a non-degenerate simplex, none of the lines exist such that they are collinear. A simplex of this form therefore encloses a finite n dimensional space or volume. Examples are a 2 dimensional triangle and a 3 dimensional tetrahedron. Choosing one of the $n + 1$ points as the origin, the n lines which originate from that point define vectors that span the n dimensional space. For the purposes of calibration, one would like to minimize the likelihood function $\mathcal{L}$ for the contents of

the bins. This is equivalent to minimizing the χ^2 of Poisson-distributed events, which is a discrete frequency distribution that gives the probability of events occuring within a fixed time interval. The method for minimization of the likelihood, as defined in the code, again employs a numerical procedure for the incrementation of parameters which specify the 'chosen points'and associated vectors:

1. Start with an initial guess V_0, and increment the vector sizes in each dimension, e_i. This defines the simplex, where all of the vertices are specified by

$$V_i = v_0 + e_i \qquad (4.24)$$

2. Carry out a series of incrementations that transform the simplex by expansion and contraction in n dimensions. These can also include a group of transformations which reflect the largest function value through the opposite face of the simplex. Under reflection, the new point is kept if the function value is reduced. The simplex must be expanded if, under both reflection and expansion, the function value at the new point is the smallest of all of the points. For both reflection and contraction, a smaller incrementation is used in the direction of function value increase.

3. After a combination of these tranformations, the simplex may eventually enclose a minimum and contract around it. This can occur until the function value within the simplex is minimized.

4.2.5   Calibration Module Details

Other code is used to provide for logarithmic energy corrections, direct calibration operators,[4] statistical error calculations, and for manipulation of auxilliary matrix elements and vectors.

---

[4] A CalD dot operator has been defined. The application of this to cluster and bump energies and angles enables the results of the calibrative procedures to be immediately plotted in histograms

The above member functions of the classes `EmcMakeABsCalPiO` and `EmcABsCAlPiO` define algorithms which are fundamental to the requirements of the background reduction investigation. Prominent examples of calibration functionality are provided by the separate fitting of the background with an exponential polynomial function, and of the peak with a bell-shaped Gaussian curve. Here, the parameters are incremented such that the background is carefully excluded from the peak fitting region. Charged tracks, bump matching and neutral cluster isolation algorithms are given with the detector geometry of the endcap and barrel specially defined, so that charged track positioning and vertexing can be compared to the angular positions of clusters and bumps.

4.2.6 The Calibration Database

The *BaBar* Calibration System is a toolkit of classes designed to implement calibration. It is not a framework like the offline reconstruction and analysis frameworks, but provides tested interfaces and implementations for developers to use. It divides the calibration procedures into a series of logical steps, and it is versatile enough to be used for processes like electronics calibration and Prompt Reconstruction. Included in the toolkit are classes to facilitate database storage, calibration data retrieval, the comparison of calibration constants and the modification of calibration data. Although the module `EmcCalPiO` used in the the π^0 calibration procedure for unreconstructed data does not utilise this toolkit, the calibration constants produced by the process can ultimately be placed into a database based upon the Calibration System. This database has been implemented by D. Brown of LBL and has been optimized further for π^0 calibration data by P. Strother, in the introduction of a new calibration class `EmcCalibrator`.

It is divided into several packages for dual, offline and online use. The package `BbrCalib` is an example which contains most of the base classes used throughout

the calibration system. The system can operate by storing the calibration constants in a database, `CalDatabase` which defines the base classes for the storage of calibration data. Before this happens, the correct data has to be extracted and analysed. C++ objectivity provides an efficient method of performing this procedure, because calibration data is irreplaceable once lost, and any subsequent analysis is essentially meaningless if the objects have not been properly calibrated. In this way it is possible for a user to apply the correct calibration procedure, such as energy calibration, to physics data. The user can then choose which set of calibration coefficients and which data to finally use.

Any calibration constants measured at a particular time, that have been found to change over a certain timescale can be stored safely in the database. The correct calibration data can then be used in a future analysis. The module `EmcCalPi0` does not output any calibration correction coefficients directly into the database at present, but could be modified later to provide real, not Monte Carlo *simulated* data calibration. Currently, energy calibration constants for use in reconstructed analyses are outputted to the database from Bhabha physics events. With real physics data, a direct interface for calibration coefficients to be inputted to the database for π^0 calibration runs, perhaps using the Calibration System would prove to be advantageous.
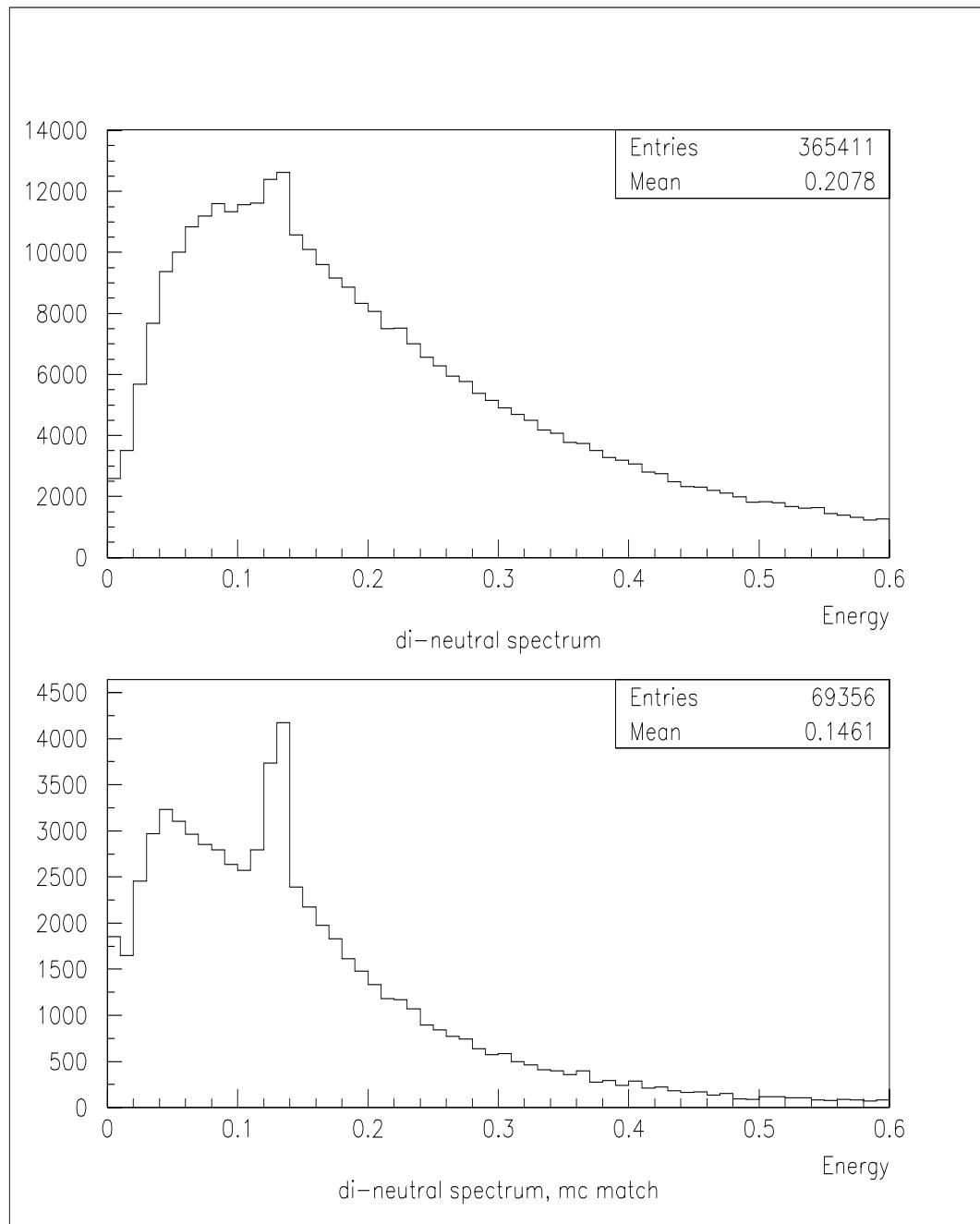
Figure 4.1: Dineutral spectra for BetaUser analysis

$\gamma\gamma$ Invariant mass cut	Efficiency
0.110 GeV $< M_{\gamma\gamma} <$ 0.160 GeV	0.90

Table 4.1: $\gamma\gamma$ invariant mass cut and efficiency
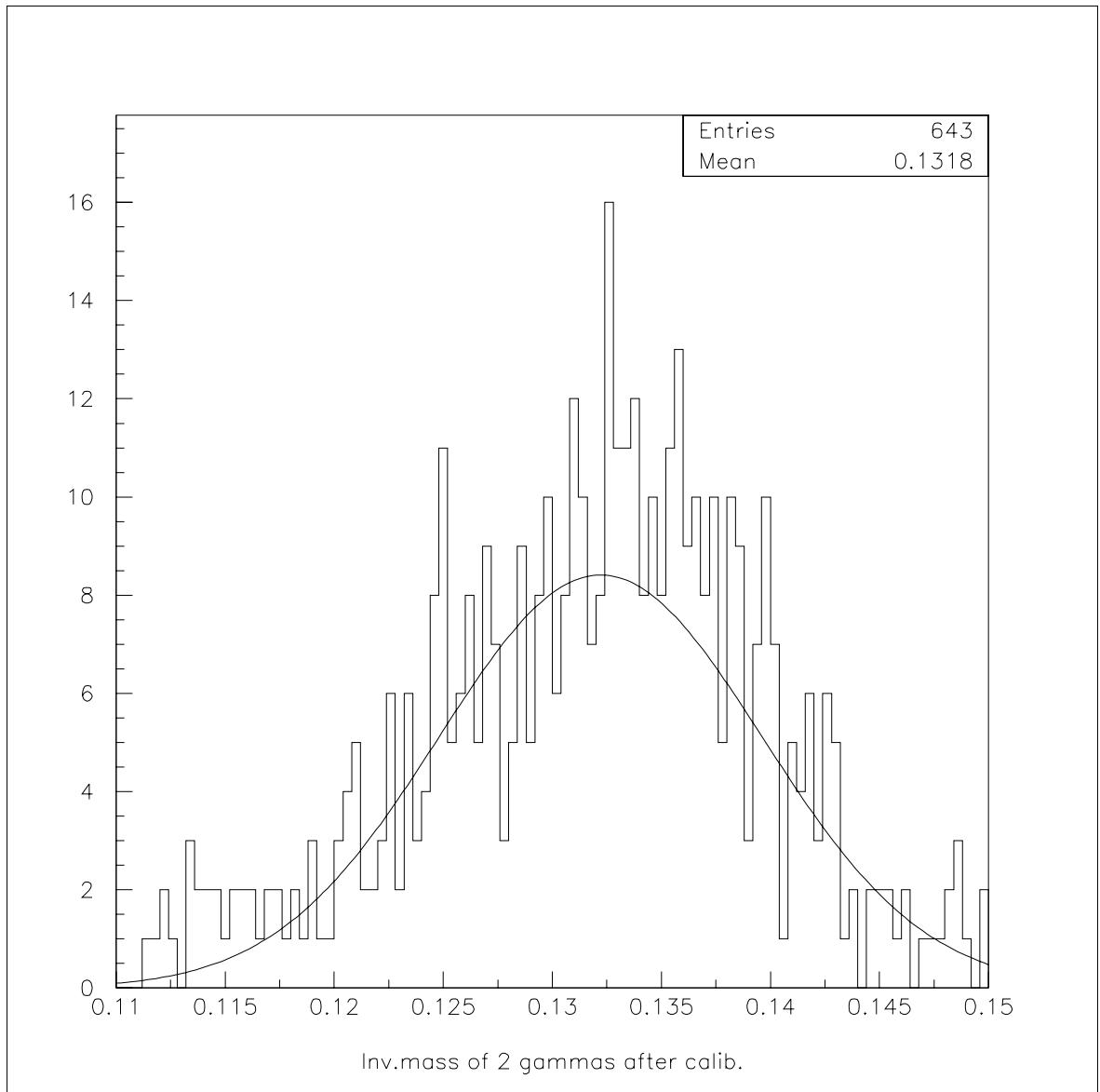
Figure 4.2: π^0 invariant mass peak from combined neutral clusters

Cluster energy range	Total number of clusters formed
0.0 GeV < energy < 1.0 GeV	49
1.0 GeV < energy < 2.0 GeV	23
2.0 GeV < energy < 3.0 GeV	22
3.0 GeV < energy < 4.0 GeV	7
4.0 GeV < energy < 5.0 GeV	9

Table 4.2: Number of clusters formed
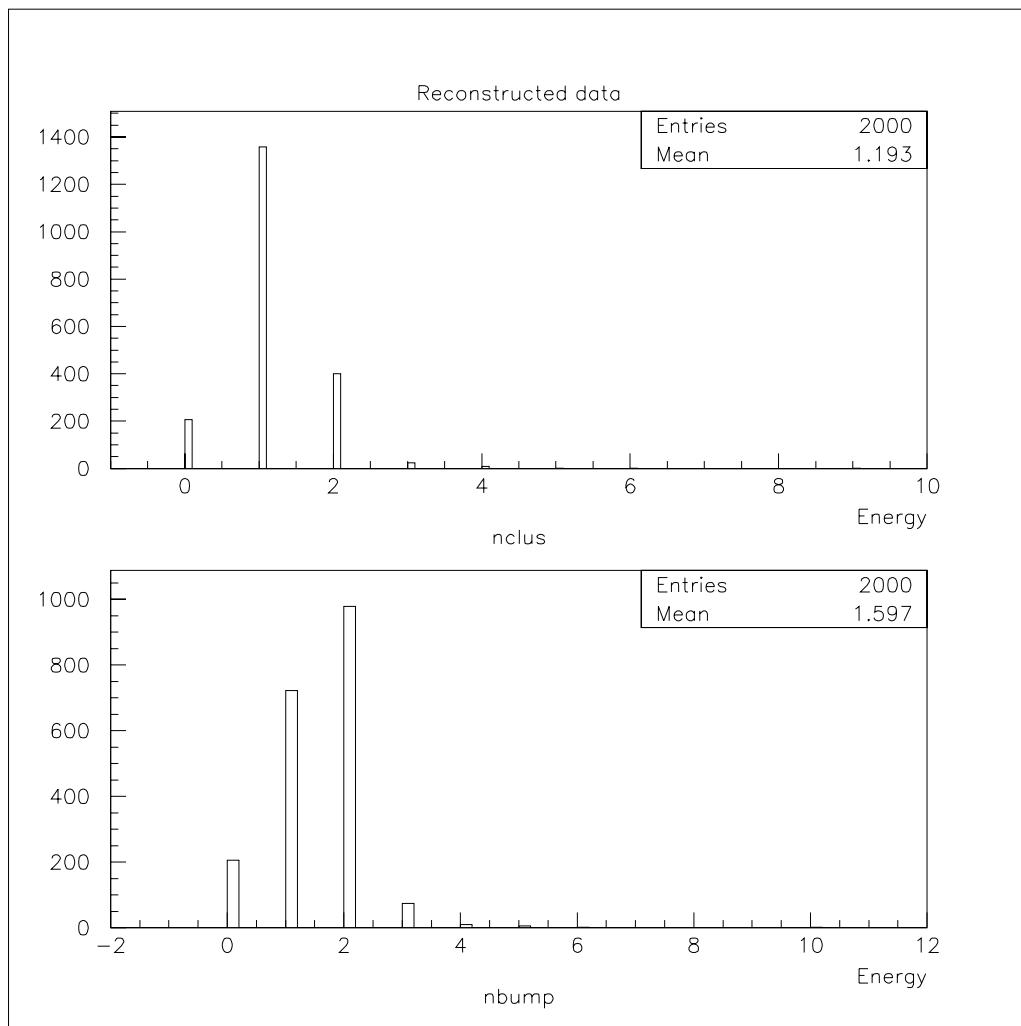

Figure 4.3: Number of clusters and bumps found in reconstruction

Minimum likelihood estimation	Value of likelihood at minimized point
0.00108	1.61547
0.00021	0.00756

Table 4.3: Typical likelihood values
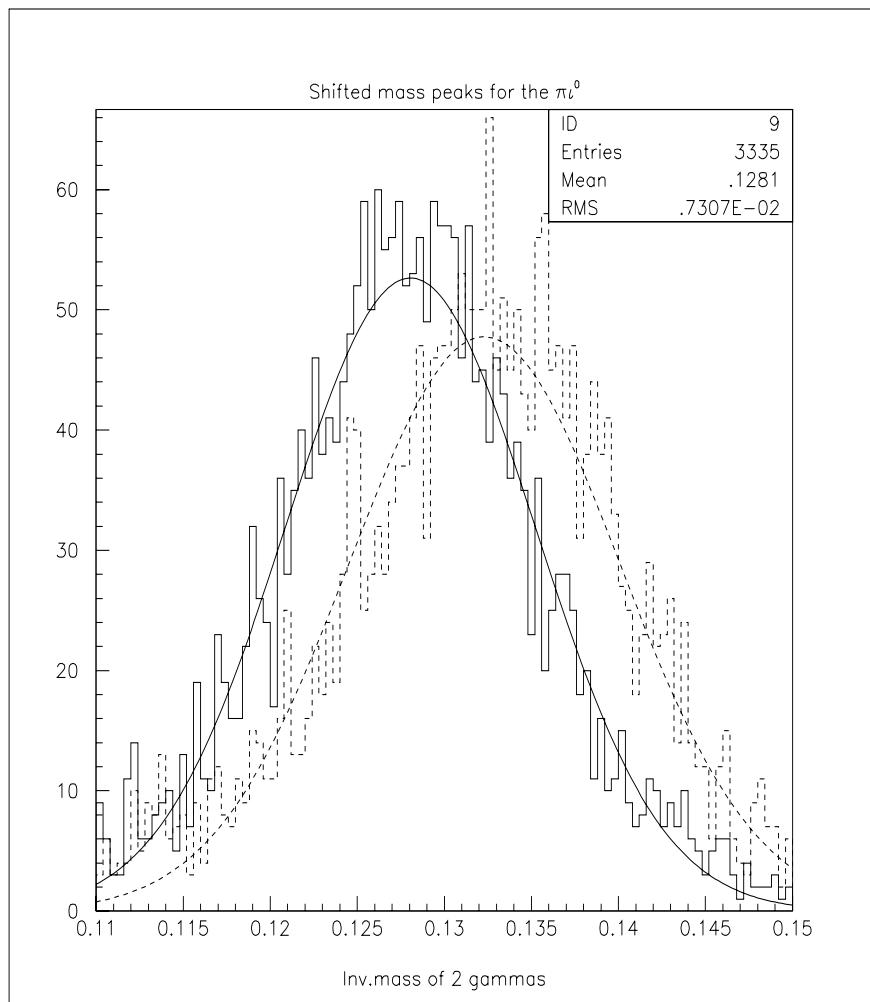


Figure 4.4: Shifting the invariant mass peak
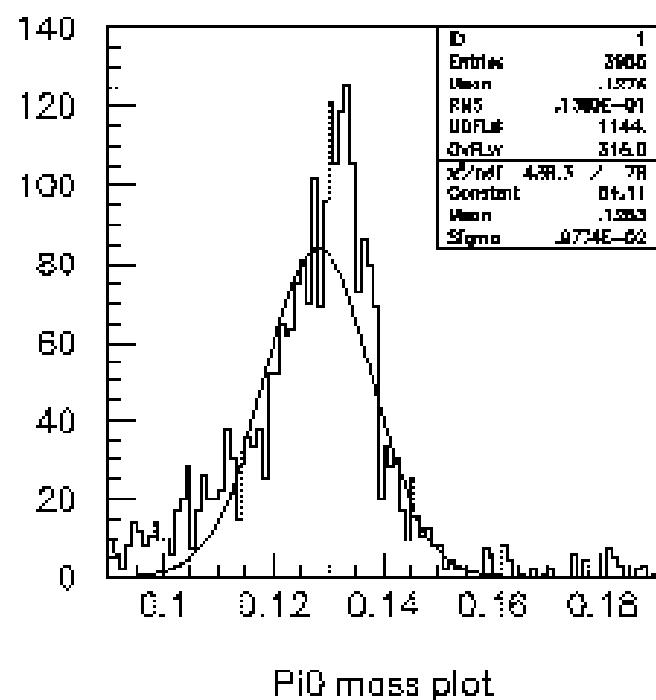
Figure 4.5: Results for one iteration of the peak

Chapter 5

CLEO II and Crystal Barrel Calibration

5.1 Calibration of Crystal barrel and CLEO II

The idea of constraining the π^0 mass peak using the energies of pairs of photon clusters is not new. The experiments CLEO II, Crystal Barrel and OPAL have all utilised this particular technique[15] [22] to calibrate their electromagnetic calorimeters. A review is given here of the methods used in the electromagnetic calorimeter energy calibration of both CLEO-II and Crystal Barrel, whose EMC's have very similar specifications and designs to that of *BaBar*.

5.1.1 CLEO-II

The CLEO-II experiment has similar goals to BaBar. It aims to make measurements of many of the CKM matrix elements, and to provide useful data on aspects of B physics. It's EMC has a barrel and endcap section containing 7800 CsI(Tl) crystals, with a prominent difference from *BaBar* arising due to the layout

of the endcap crystals. These are not organised radially into modular units, but are structured into columns and rows by quadrants.

At energies of ~ 5 GeV, photons are calibrated by constraining Bhabha showers to the beam energy. Below 5 GeV and down to approximately 0.5 GeV, photon energies from radiative QED events are analysed. For this energy scale, use was made of the fact that for radiative events, the photon energy can be constrained from the angles and track momenta. Deviations for various physics events were found to be consistent with one another, and amounted to a small correction at the 0.20% level. The energy scale below 500 MeV has been calibrated using both π^0's and η's. The π^0's cannot be used to calibrate using the same methods as for radiative QED events because not every π^0 candidate is real, and there are two photons per π^0. The calibration is therefore done on a statistical basis, so that both constituent energies are accounted for. CLEO have adopted a convention whereby[17]

"the peak energy should be at the true incident photon energy."

In effect, the CLEO calibration approach aims to provide an incorrect value for the mass, but with the discrepancy being correctly accounted for by the data and Monte Carlo comparison.

Again, because of the effects of the clustering algorithms, electronic noise and photon shower leakage CLEO have found that the π^0 photon lineshape is asymmetric about the peak, with an efficiency related low-side tail. They have observed that even for perfectly calibrated photons, the $\gamma\gamma$ mass peak will be found at a position *below* the expected mass of the π^0. Although the photon peaks may be accurate, the low side tails cause the π^0 mass to peak below nominal. CLEO have noted that because the tail varies with energy, the extent to which the π^0 mass peak is found to be below the nominal energy is governed by the energies of both photons. These are termed E_{lo} and E_{hi}.

As a consequence, CLEO have performed the π^0 calibration using the fol-

lowing steps:

1. Use the Monte Carlo data to generate a 2 dimensional grid, in E_{lo} and E_{hi} bins of expected π^0 masses for perfectly calibrated photons. This grid shows a discrepancy in the π^0 mass peaks from 0.2 to 0.9 MeV below the nominal π^0 mass, resulting from the photon energies.

2. Prepare $\gamma\gamma$ mass histograms from the data for each E_{lo}, E_{hi} bin. The cuts on selecting candidates are used to maximize the probability that the photon shower is not overlapped by any other showers, and that the neutral showers are isolated away from tracks and have lateral shape consistent with photons.

3. Fit each 2 dimensional bin with a curve matching the expected photon lineshape, using a polynomial background and the peak as a free parameter. This produces 2 dimensional grids containing the expected and measured π^0 masses.

4. Extract from the data and Monte Carlo comparison the photon energy correction factor, using the measured and expected masses.

The CLEO II collaboration managed to achieve an absolute energy calibration, 'semi-globally' over their calorimeter to better than 0.5%; the π^0 calibration was never done for the endcaps. An energy dependent factor was also found in the region of $1 - 3\%$. No angular dependence was observed within the barrel because statistics were limited; the π^0 mass width was found to be dependent upon both the photon energy and angular resolution.

5.1.2   Crystal Barrel

The aim of the Crystal Barrel experiment at CERN is to observe $p\bar{p}$ annihilations at rest. An array containing 1380 CsI crystals has been constructed to provide calorimetry for decaying η, π^0 and ω mesons. Crystal Barrel's π^0 calibration

procedure, which was done once every one to three weeks, differed in approach to the method used by *BaBar* and CLEO II.

Hits were used to calibrate the crystals on a local, individual basis. Charged clusters were separated from those caused by neutrals by using a cut placed on cluster size, which was found to be dependent upon energy. Cuts were applied first on cluster energy, and on the number of photons observed. Events were selected which contained no more than 8 photons. This was claimed to reduce the combinatorial background.

Histograms of invariant mass were then produced for each crystal which recorded a photon, and all mass-squared values were considered, by pairing the measured photon in sequence with all of the other photons found in the events. A pre-calibration, using a minimum ionizing peak method was required. So, each crystal had a pre-calibration factor and an invariant mass peak. To save time, a level two software trigger was used to decide on events for the calibration dataset. This had a 6 dimensional look-up table, which held invariant mass, energy and space-angular information for every possible pair combination. π^0 and η mesons could be selected within a 50 MeV mass window.

In effect, the Crystal Barrel method first localised the peak position using another calibrative method. The application of Chebyshev polynomial fits to the peaks ensured that the peaks could be iterated back to their proper places; the peak position being largely dependent upon the pre-calibration factor determined.

The Crystal Barrel calorimeter achieved a mass resolution of $\sigma(m_{\pi^0})$ Of 9.9 MeV, with experimental data in agreement at the lower energy scale to a $1/\sqrt[4]{E}$ dependence.

Chapter 6

Analysis, Results and Conclusion

6.1 Results and Analysis

In an ideal world, no background processes would be available to contaminate and mimic important physics events, and all physics analyses would have a reconstruction efficiency of 100 %. The reality is that background events are as unavoidable as quantum uncertainty. Ways must therefore be found to efficiently reject, reduce or estimate background events.

The possibility of $\Upsilon(4s)$ background reduction, for energy calibration with small datasets and hence small statistics was investigated. At present, relatively large numbers of events are needed[1] to perform the π^0 calibration. This amount of data has to be collected over a timescale $\sim$ 3 - 4 weeks. The long timescale involved means that studies of the short term behaviour of crystal response are effectively excluded. However, long term effects resulting from radiation damage and crystal ageing, may be noticeable from any observed long term changes in crystal calibration constants.

---

[1] For π^0 calibration $\sim 1 \times 10^4$ events are required

The background reduction investigation was done under the assumption that the methods described which find, iterate and produce correction coefficients from the π^0 peak were already working correctly.

Two main decay modes were used to compare the performance of the calibration code, under clean and background-contaminated conditions. The modes considered were the Mock Data Challenge BEAST tape events $\pi^0 \rightarrow \gamma\gamma$, and $\Upsilon(4s) \rightarrow B^0\bar{B}^0 \rightarrow Q\bar{Q} + X$, where X constituted background. If the background could be reduced for the actual $\Upsilon(4s)$ run data, then the π^0 peaks would be defined with greater clarity, and the efficiency for π^0's would be increased[18]. This would allow the uncalibrated peak position to be located more precisely, leading to the production of more accurate calibration constants.

The first step was to ensure that clean π^0 peaks could be found. Ntuples could then be written to investigate the results and workings of the clustering algorithms for the unreconstructed data. Using $\pi^0 \rightarrow \gamma\gamma$ data, various cuts were tried until the best peaks were seen. The efficiency for the production of a prominent π^0 peak is determined by a cut on the $\gamma\gamma$ mass, the value of which depends upon the background level for a particular process [19]. Various mass cuts were tried, and the optimal mass peak - examples of which are shown in figure (6.1), was found to occur for $0.11 < m_{\gamma\gamma} < 0.15$ GeV. The next step was to observe the nature and effects of the cluster and bump algorithms, and to evaluate the performance of the calibration procedure on cluster and bump energies and the photon decay angles. This was because it was necessary to find out whether or not the cluster and bump forming algorithms were working properly.

Combinatorial background can increase if an incorrect number of clusters or bumps are summed over, because the clusters and bumps summed over should have a strict dependence on energy. The bottom part of figure (6.2) shows the unreconstructed number of clusters found at a particular energy, for the energy range 0.0 - 5.0 GeV. It can be seen that the total number of clusters summed

over decreases with energy up to approximately 1 GeV. Beyond this point, the distribution is roughly level. The number of clusters formed is found to be highest below an energy of 150 MeV. The greatest numbers of clusters are summed and combined to form π^0's, which have a distinguishable peak above the continuous $Q\bar{Q}$ background. No notable increase was seen in the number of clusters, at an energy favourable for η meson production.

With increasing π^0 energies, the space angle between the two decay photons will decrease, in accordance with equation (2.25). This means that at lower energies, we expect to see more individual clusters in the calorimeter. At higher energies small space angles, η cause the photons to cause neutral showering over a smaller angular region in the calorimeter. It is therefore expected that at higher π^0 energies, more bumps will be found by the action of the bump-forming algorithms. A cluster can begin as a CR (connected region of adjacent crystals), and it may be separated into 'bumps' if it contains a local maximum of energy deposition. A bump is a CR or part of a CR that is associated with a single particle interaction, such as a photon.

6.1.1   Considering Clustering Strategies

To see whether the cluster and bump forming algorithms were working correctly, it was decided that the number of bumps and clusters formed should be investigated, as a function of energy. Figure (6.3) implies that bumps are really clusters that are merged together by the clustering algorithms. These histograms were created using unreconstructed data, and they display how many individual bumps or clusters, pairs of bumps or clusters and groups of three bumps or more were found in the calorimeter, for 2×10^3 events. The bottom part of figure (6.3) shows that, with energy decreasing to the left, the number of individual clusters found at low energies is greater than the number of individual clusters found at higher energies. The top part of the figure is not as well understood. Although

most of the bumps are found in pairs, as in figure (4.3), the reason why more bumps are not seen at higher energy (with energy increasing to the right of the plot) is unclear. It could be that the 2 dimensional algorithm, which forms clusters from bumps was not functioning properly in this case, or that higher statistics were needed.

The effects of energy calibration on the bump energies were then checked. The aim of the calibration procedure is not only to get the π^0 mass peak in the right place,[2] but to correct the photon energies measured by the calorimeter. If the mass peak is shifted to 135 MeV and the resultant photon energies are found to be incorrectly calibrated, then perhaps the correct peak position is that which determines the actual mean, mode or median of the photon energies. The ratio of the calibrated energies of the bumps to the uncalibrated bumps energies were plotted in figure (6.4). The first and second bumps corresponded here to the two 'individual' π^0 decay photons. The ratios $E_{\gamma 1}^{cal}/E_{\gamma 1}^{uncal}$ and $E_{\gamma 2}^{cal}/E_{\gamma 2}^{uncal}$ were plotted as ntuples, where the pointers

```
en1 = theBump1->energy()      en2 = theBump2->energy()
```

were used to access the uncalibrated bump energies. Similar pointers were used for the calibrated bump energies; the calibration was applied through the use of the `CalD` calibration dot operator to the `en1,2` photon energies.

As the peaks are narrow, the difference between the calibrated and uncalibrated bump energies must be small, despite the small tail found for the first bump ratio. Figure (6.5) shows the number of bumps against energy for both calibrated and uncalibrated bump E_1 and E_2's, where the number of bumps found has the same form of decreasing energy dependence as for the cluster histogram in figure (6.2). For the same number of events, there was clearly a deficit in the total number

---

[2]this would be beneficial to reconstruction efficiency in physics analyses, if the calibration constants produced a good fit

of entries binned between the first and second bumps. A possible explanation is that the second bumps should usually be found to contain an energy below 1 GeV.

6.1.2 Photon Candidates

A plot of the number of individual hits, which are the raw materials from which clusters and bumps are formed, has been plotted as a function of bump energy, (figure 6.7). The increase of the number of hits with bump energy is apparent, where the total number of hits at any bump energy seems to be confined to a scattered region of 0 to 100. At higher energies more hits are expected to be found, with the energy of bump split-offs increasing as local maxima contain more energy, from increased showering over more crystals. A two-bump CR with an energy of 500 MeV is most likely to be caused by random overlap, but one with an energy of 3 GeV is most likely to be caused by a π^0. Cuts on bumps, for the summation of energies above 1 to 2 GeV should therefore minimise the probability that a bump pair was not caused by a neutral π^0.

To investigate this bump merging behaviour, a comparison of the Monte Carlo π^0 truth energies with the number of bumps formed would be beneficial. Figure (6.8) shows the π^0 mass, (derived from the π^0 energy) plotted against the bump energy found. Below bump energies of aproximately 200 MeV, spurious background can be observed, caused by the summation of bump pairs which need not be summed. In this region, the π^0 mass is not well defined. Above 1 GeV, the scattered points are observed to lie in a π^0 mass range of 0.15 ± 0.025 GeV. Figure (6.6) [20] gave further indication that the bump and cluster forming algorithms were not working as efficiently as expected. This conveys the energy discrepancy seen in the Monte Carlo data, for the energy of the 'photon' candidates and their GEANT ancestors. The 'photon' candidate energy is plotted against the MC truth energy, resulting in a clear linear relationship between the two variables. Toward the base of the

histogram horizontal bands can be seen, which are due to the presence of charged minimum ionising particles (MIP's). These have an energy ~ 200 MeV. Considering the energy losses of minimum ionising particles in the CsI crystal medium, where $dE/dx|_{min} = 1.243$ MeV g^{-1} cm^2, and the density is 4.51 g cm^{-3}, a 35 cm crystal will have a minimum ionisation energy of 196 MeV [21]. These particles must not be included in bump pair combinations, as they affect the tail and hence the mass resolution of the π^0 peak, and contribute greatly to unwanted background.

6.1.3 Finding the Peak

The Crystal Barrel Collaboration [22] have noted that the η peak, corresponding to a mass of 547.5 MeV, appeared when the continuum background level was reduced. A method of accurately determining the position and mass resolution of the η peak, in amongst the background would be highly beneficial to the calibration procedure. The careful application of cuts, or a reduction of the $\Upsilon(4s)$ continuum background could enable the calibration code to resolve a good η peak. The method of photon energy calibration, whereby both the η and π^0 peaks are iterated simultaneously would then be possible.

During the analysis of the decay $\pi^0 \to \gamma\gamma$ above, no η peaks were found. A different method, which could be used to measure the accuracy to which the π^0 peak has been shifted to the proper place, or perhaps even to find the π^0 and η peaks in a large amount of background is described below. Consider a pseudoscalar meson decaying at rest to two photons (equation 2.25); the invariant mass equation is relevant for both η's as well as π^0's and can be rewritten as

$$\frac{m^2_{meson}}{2E_1E_2} + \cos\eta = 1 \tag{6.1}$$

Re-arranging this gives an equation which is linear in form.

$$\cos\eta^0 = 1 - \frac{m^2_{meson}}{2E_1E_2} \tag{6.2}$$

Plotting a histogram of $1 - \cos \eta$ as ordinate, against $1/(2E_1 E_2)$ therefore gives a linear straight line, with an intercept of zero and where the fitted gradient is equal to the invariant mass squared of the pseudoscalar meson. This method can be used to both identify and distinguish between the η and π^0 candidates. The results are shown in histogram (figure 6.9) and lego plot (figure 6.10).

6.1.4   Fitting Background Events

To investigate the effects of background on the ability of the code to find the peak signals, and to evaluate the proportion of background present further events were processed. These were done using the relatively clean decays $B^0 \rightarrow \pi^0 \pi^0$, $\bar{B}^0 \rightarrow \nu \bar{\nu}$ and the decay $\Upsilon(4s) \rightarrow Q\bar{Q} \rightarrow X+$ background so that the effects of background could be evaluated, and so that methods of background reduction could be applied. The results for invariant mass histograms for the decays $B^0 \rightarrow \pi^0 \pi^0$, $\bar{B}^0 \rightarrow \nu \bar{\nu}$ where two π^0's were looked for, are given in figure (6.11). These show that the ratios of the invariant mass of the two photons to the π^0 mass are shifted closer to the true value, after calibration has been applied. Since the $\bar{B}^0$ decays to neutrinos, these events have 'missing energy' but little background. The lower histograms give the results for the ratios of the calibrated and uncalibrated invariant masses of the two photons found, over the expected mass of the η meson. No peak is really discernible here; the η decays have provided too few events. Larger cuts on invariant mass, in the range $0.0 < m_{\gamma\gamma} < 0.65$ GeV could help the η peak to be found, but the π^0 peak would not be as prominent. The decays $\Upsilon(4s) \rightarrow Q\bar{Q} + X$ were used for the background investigation. The same form of plots as for the above were done for these background events, and the results are shown in figure (6.12), where no plots for the η peak are shown as none were found. The top and bottom histograms are the same and were produced using simple cuts, where $0.110 < m_{\gamma\gamma} < 0.160$ GeV. The fits to the top two histograms are polynomial, to fifth order. The fits to the bottom two histograms are gaussian. The histograms at the top show a peak forming amongst

continuum background, which has successfully been calibrated to the correct π^0 value, if the polynomial fits are to be believed. The gaussian fits do not seem to fit well, and the polynomial fits diverge asymptotically at the edges, where the second derivatives of the function should be zero. This is one reason why the peak and background must be fitted with gaussian and exponential or logarithmic polynomial (not Legendre polynomial-like Chebyshev) functions, respectively. Marsiske et al. [23] have shown that the rejection of charged tracks before neutral cluster summation has resulted in a four-fold background reduction.

6.1.5 Charged Track Rejection and Angular Resolution

For effective background reduction, the clusters and bumps which are combined to form π^0's should be:

- isolated from other neutral clusters at energies approaching 2.5 GeV

- not near any charged tracks

- consistent with photons in lateral and longitudinal shower shape and total energy deposition

If any of the neutral clusters do not agree with the above criteria, they should not be included in the final iteration over photon clusters.

In the calibration module, due to the relativistic boost in the centre-of-mass frame, the space-angle α is defined in terms of functions containing transformations of the angles θ and ϕ. Pointers to the θ and ϕ cluster angles were used for the purposes of neutral cluster and charged track isolation in the background rejection algorithms. These functions were looped over separately in the code and were compared individually, to the value given for α calculated by the invariant mass equation. One good reason for defining the angles of the clusters and bumps in this

way was that the resolution of the detector could be incorporated easily into the cluster isolation algorithm. If clusters did not fulfill the selection criteria defined in the code, then they were not listed as neutral clusters and were not included in any further combinatorial or iterative processes. The inequality [23]

$$\left(\frac{\theta_{clus} - \theta_{track}}{10.0}\right)^2 + \left(\frac{\phi_{clus} - \phi_{track}}{20.0}^2\right) < 1.0 \qquad (6.3)$$

was used to reject charged tracks when the θ and ϕ angles between the track and neutral cluster candidates were small. The denominators specified in equation (6.3) above characterize the angular resolution in θ and ϕ for the electromagnetic calorimeter. The intrinsic resolution in ϕ must be greater than that for θ, because of the bending of the charged tracks over this angular region in the solenoidal field.

These particular values may not have been accounted for correctly, with respect to the expected low angular resolution behaviour. As the calorimeter is finely segmented with respect to the dimensions of each crystal block, the angular resolution is expected to be much greater than that of CLEO-II's electromagnetic calorimeter, with an expected resolution of $\sigma_\theta \simeq 4.25$ milliradians at $\cos\theta = 90^0$. This resolution, achieved by the smaller transverse crystal sizes, the longer distances encountered to many of the crystals and much lower electronic noise, is found to decrease as the angle θ (in the laboratory frame) increases. Although the previous may compensate slightly for the increased staggering of the crystals,[3] as θ increases, the angular resolution is still degraded somewhat by the nature of the weighted centre-of-gravity, and other similar cluster positioning algorithms, within individual blocks. The target angular resolution is:

$$\sigma_\theta = \frac{3\mathrm{mrad}}{\sqrt{E(GeV)}} \oplus 2\mathrm{mrad} \qquad (6.4)$$

where the design performance target for σ_θ at 1 GeV and 90^0 is 5 milliradians.

Accounting for these, a reduction of the values of the denominator in equation (6.3) could have improved the background reduction, if the resolution was set

---

[3]The projective geometry encountered in the endcap also affects resolution

to values closer to those required by the design performance targets. The results, with and without the denominator value changes by 5 and 10 milliradians respectively, are shown in figures (6.13) and (6.14). Unfortunately, the total number of entries for each histogram is not the same. The histograms cannot therefore be compared for any sign of a reduction in background, or for the development of a significant peak. Polynomial fits to 15th order indicate that an 'emerging' peak has been shifted to the right after calibration.

6.2 Conclusion

The Manchester and Liverpool *BaBar* groups have successfully constructed the twenty endcap modules needed for the EMC endcap. The calorimeter should take its first data with cosmic rays before spring 1999. Positive results from a calorimeter testbeam study have indicated that the calorimeter will achieve the required performance targets.

Low noise electronics and finer segmentation should enable *BaBar* to achieve an absolute energy calibration over the barrel and endcap regions comparable to, or better than CLEO II's 0.5 %. For these reasons, the calorimeter should have excellent energy resolution, although it remains to be seen whether the real data will be consistent with the Monte Carlo expectations.

From the bumps and clustering results, the algorithms seem to be working well, but they do not seem to be performing as efficiently as they could. The charged track and neutral cluster isolation algorithms have previously reduced the background by 3 to 4 times. It seems that too many charged particles, such as M.I.P's are evading the neutral cluster isolation and charged track rejection algorithms. The Monte Carlo truth data for the bumps and clusters therefore needs to be looked at in more detail, so that a comparison can pinpoint the precise areas in which the discrepancies lie.

In a rapidly changing software environment, not all code works as efficiently as it should. Ongoing software package releases and continued testing will help to ensure that the desired results are achieved. The methods of cluster positioning will soon be optimised, using weighted rejection and centre-of-gravity methods.

It was realised, after the *number* of bumps and clusters had been investigated (as a function of varying energy) that measurements of the lateral shower shape of the clusters could be significant in reducing background. If the expected shower shapes for neutral clusters of varying energy and relative position were known, then these could be compared with mixed charged and neutral clusters. Questions would then be raised regarding the consistency of these measurements with neutral candidates. If the lateral shower shapes were then seen to be more consistent with electron showers than photons, then these objects could be deleted from the neutral cluster lists, before $\gamma\gamma$ combination. The histogram shown for the number of hits against photon energy is, as it were, a step in the right direction. This showed hits in individual crystal blocks which were later combined to produce clusters, at a given energy. The clustering algorithms use a random walk technique to iterate over crystal energy deposits. Lateral shower spread measurements requiring the determination of the spatial characteristics (and not just the number of), depositions are needed. Measurements of the moments and weighting of the clusters can also return four-vectors for the positions of the original particles, again useful for studies of angular resolution.

A useful method which can be used to separate both photon peaks found in a cluster involves second moments. The second moment of a cluster is given by:

$$M = \frac{\Sigma_i E_i |\Theta_i|}{\Sigma_i E_i}, \tag{6.5}$$

where Θ_i is a vector containing the angular separation in theta and phi of the ith crystal and the cluster major axis. A cluster may be resolved into its component photons using this technique.

6.2.1 Background Reduction ?

The charged track rejection and other methods used in the investigation of background reduction provided inconclusive results, as the histograms both with and without the algorithms were returned with a large difference in the total number of events. The polynomial fitted results to the background events imply that one does not necessarily have to reduce the background; it is the accuracy of the fit to the peak, amongst the background which is important. Exponential polynomial functions should be used to fit these peaks.

Fitting the peak accurately, so that it may be shifted to give an answer approaching unity for $m_{\gamma\gamma}$ / m_{π^0} does not ensure that the calibration procedure is correct. Due to the way in which the photon lineshapes are folded together, the individual photon peaks do not obey the usual rules of addition in forming a π^0 peak. If the photon energies, E_1 and E_2 are measured precisely, then the peak will not be found in the right place. If the peak is iterated to the right place, then the photon energies will be incorrect. If both the peak and photon energies can be measured correctly, then the absolute energy calibration has been successful. Reconstruction efficiency may also improve as a result. Photon energy calibration using the logarithm of the photon energies may help in this case.

The module `EmcCalPiO` worked well, but the coefficients initially used were incorrect. This had an effect on the end result calibration constants. It is possible that the calibration procedure implemented using class `EmcCalibrator` has produced better results for the coefficients, albeit utilising a simplified method. The class `TrkRecoTrk` in module `EmcReco` should be implemented. This would provide a better method of ensuring that neutral clusters are isolated from charged tracks, as information can be used directly from the tracker.

The lego plot technique could be developed further, as a method for distinguishing π^0 and η peaks from large levels of background. A proper straight line fit

to the similar linear plot would give the mass-squared of the mesons. The departure from the expected masses for the measured masses be evaluated simultaneously, if both the π^0 and η peaks could be iterated simultaneously.

6.2.2 Discussion

The aim of this thesis has been to give an overview of the *BaBar* π^0 energy calibration procedure. An investigation of the possibility of background reduction was undertaken. The results have been presented.

The local calibration procedure of Crystal Barrel, whereby each crystal was calibrated individually used 1.2×10^6 neutral events, where 3 π^0's were seen per event. Hadronic events that will take place at *BaBar* are expected to have 4 π^0's per event. *BaBar*'s global calibration procedure, where each π^0 event is used to calibrate over 6000 crystals, averaged for 15 energy bins, is expected to collect the necessary statistics for the barrel region in a day. The necessary crystal ring statistics will take longer to accumulate. For an accurate calibration of the whole detector (including the endcap), 30 to 40 days are required.

This investigation has looked at methods of decreasing the background expected for $\Upsilon(4s)$ decays. However, the primary aim of the calibration procedure is to produce accurate calibration coefficients. If the background can be reduced significantly, by perhaps another factor of 10, then certainly the peak will be found more efficiently and more accurate calibration coefficients will result. With regards to the decrease in the timescale needed, monitoring of short term variations in calorimeter response will not be possible, but short term monitoring of the calorimeter response will be provided by the light pulser system. Further investigations of the lateral shower-shape consistency, of the expected detector angular resolution, and of charged track rejection will indicate whether the timescale can actually be reduced to the order of a week, for more efficient calibration runs.
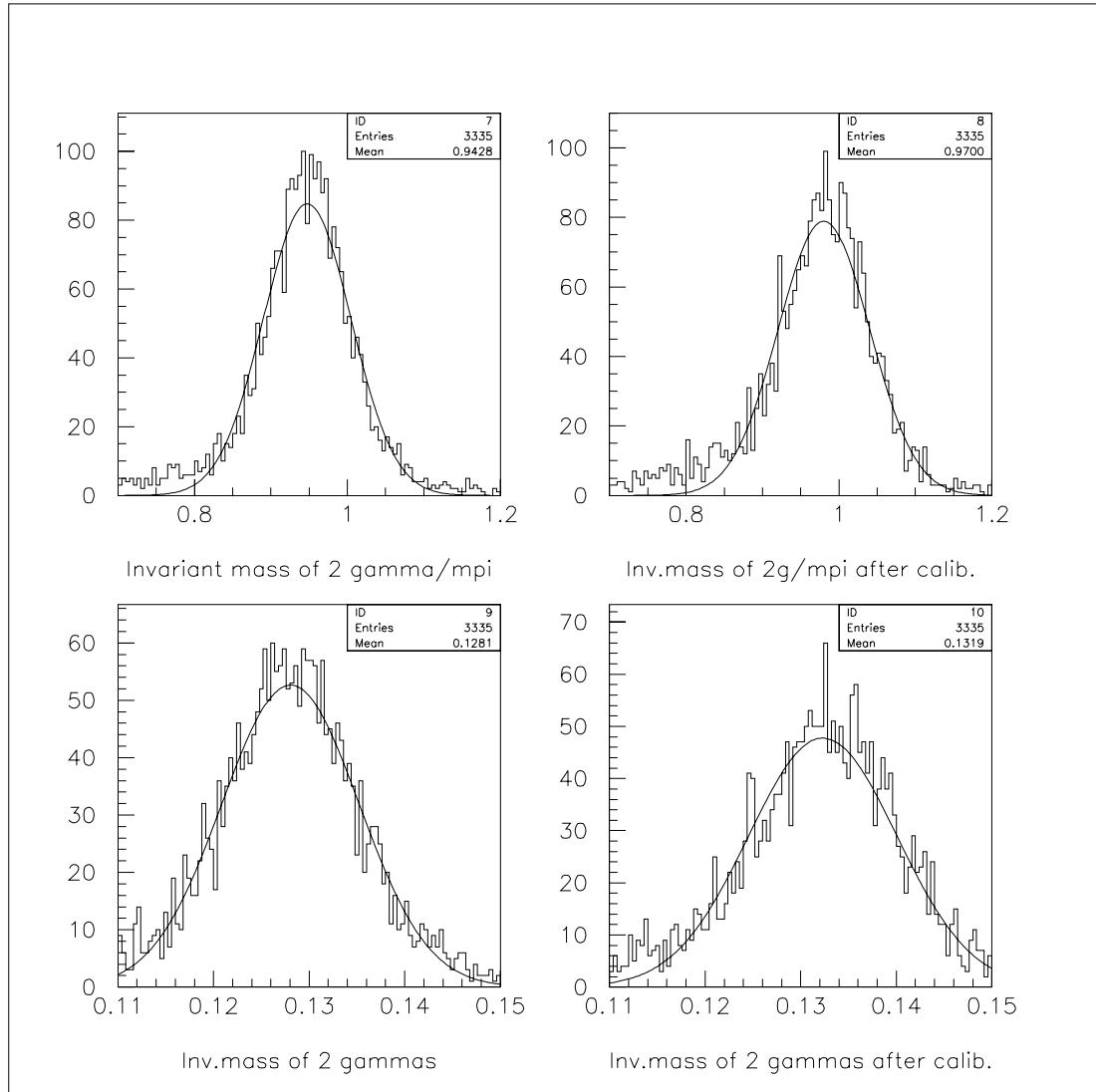
Figure 6.1: Shifted peaks for (top) invariant mass ratio and (bottom) invariant mass
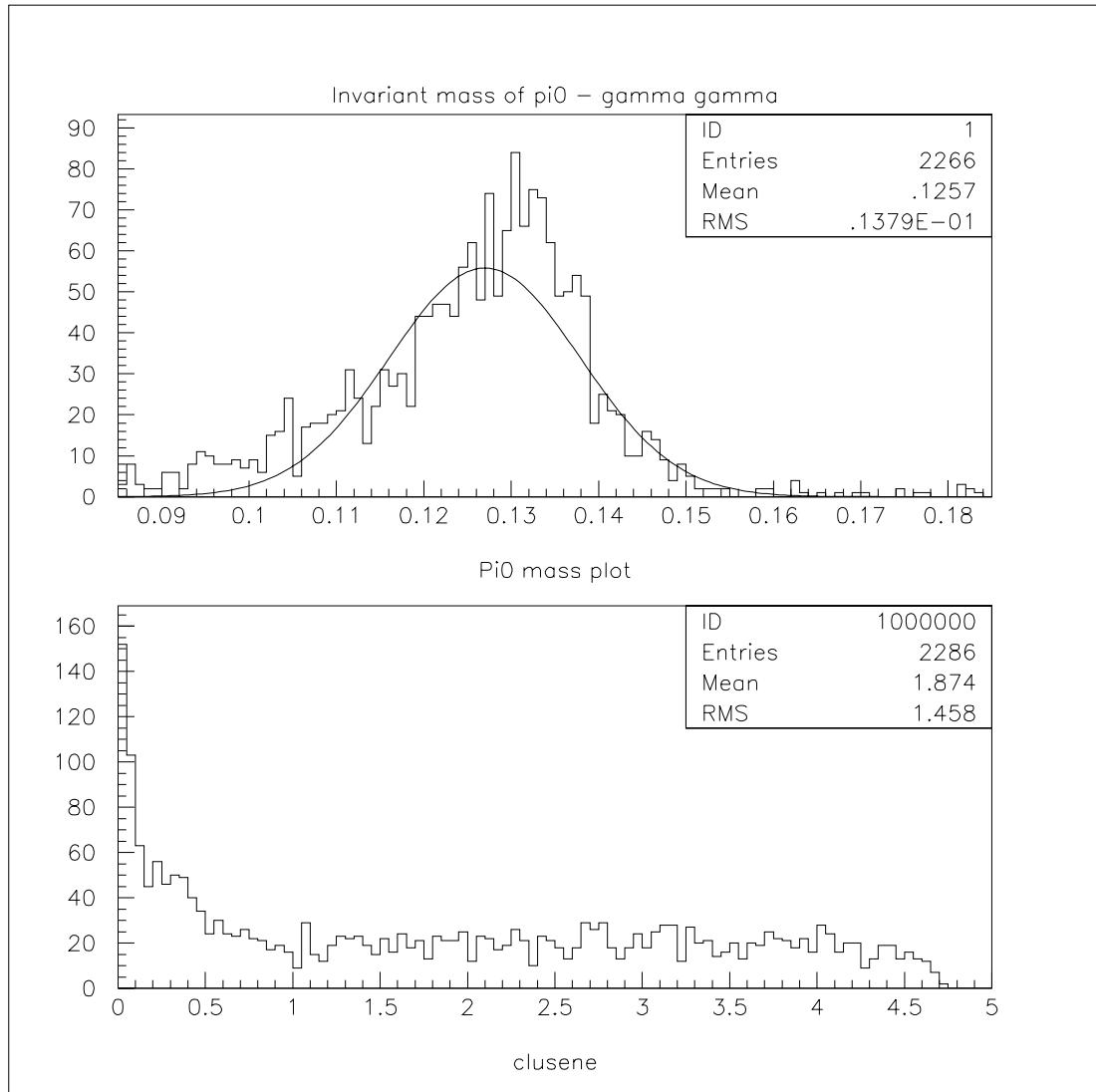
Figure 6.2: Optimal π^0 peak and cluster numbers found
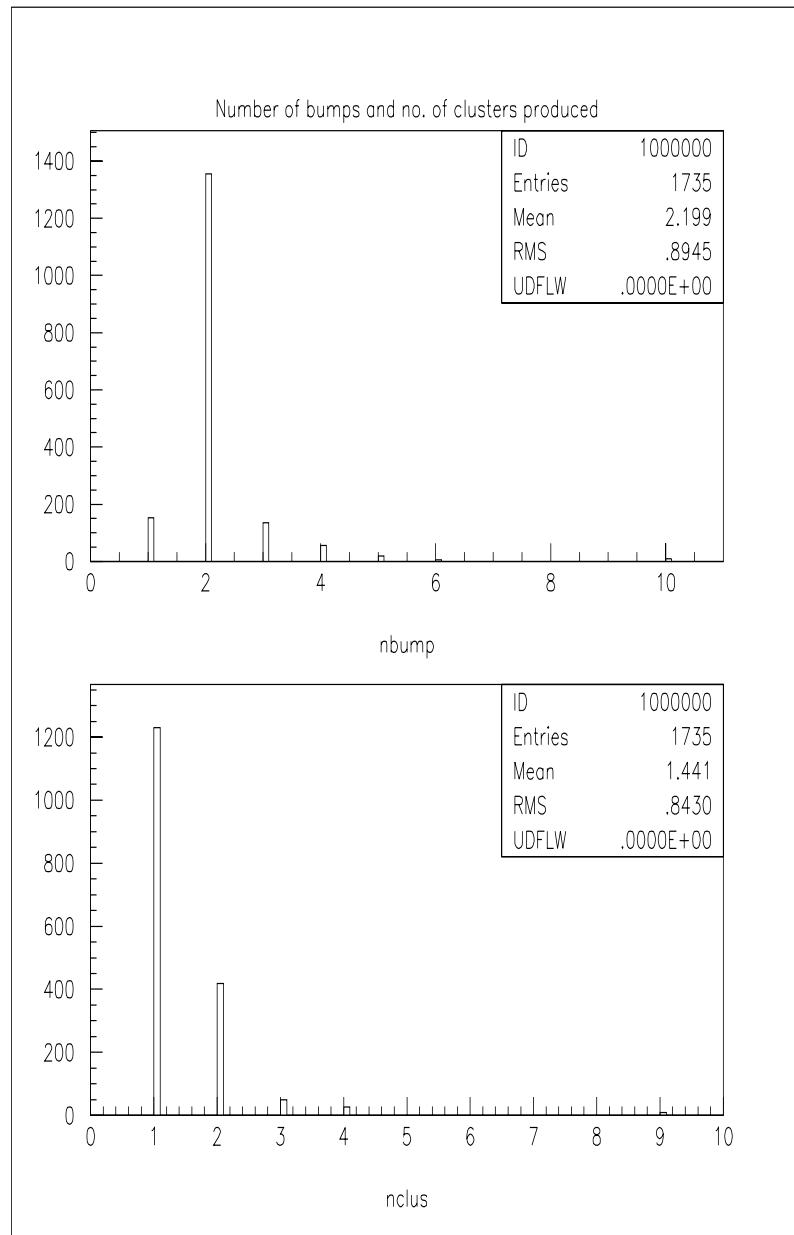
Figure 6.3: Numbers of individual merged bumps and clusters summed
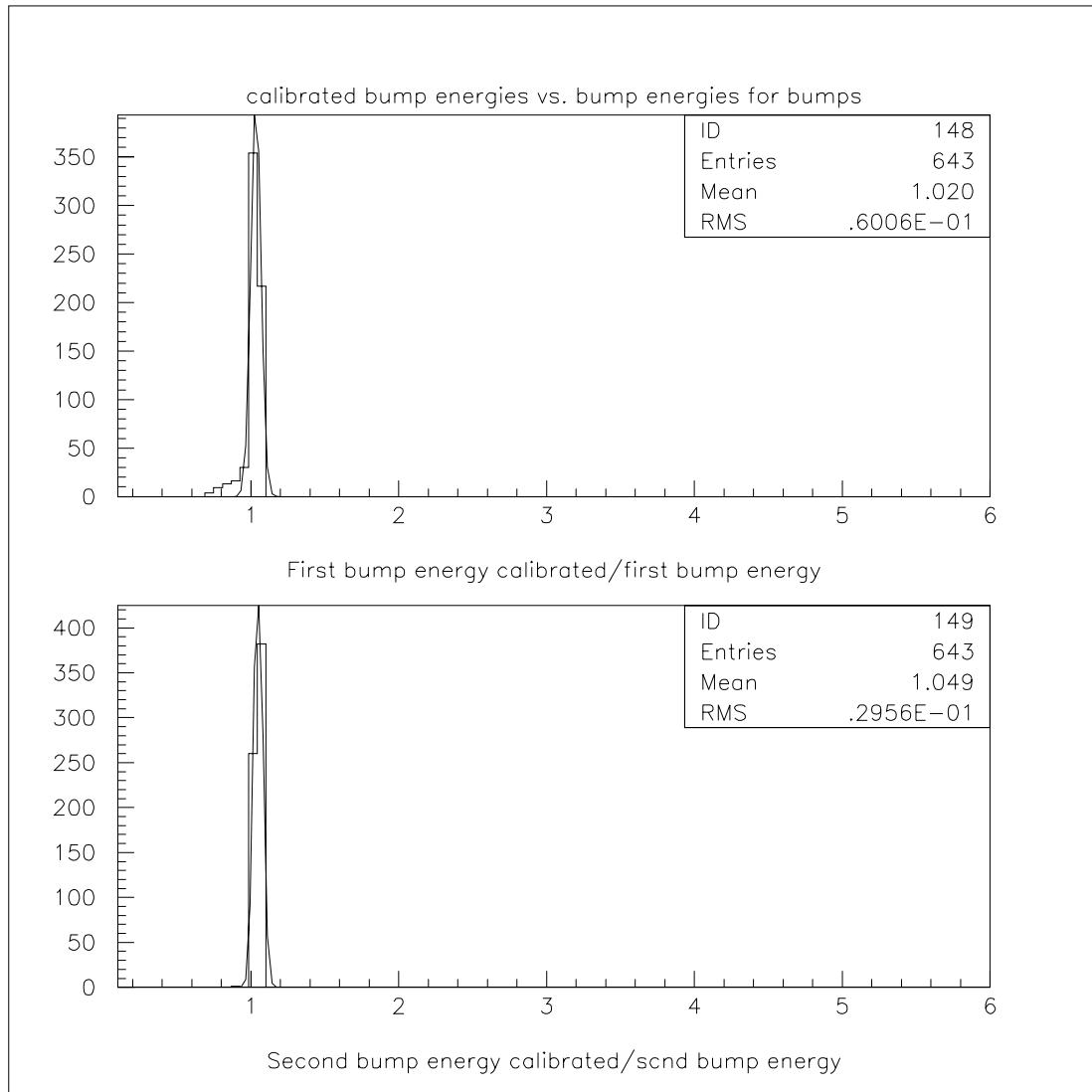
Figure 6.4: Entries vs calibrated bump energies and uncalibrated energies for bumps 1 and 2
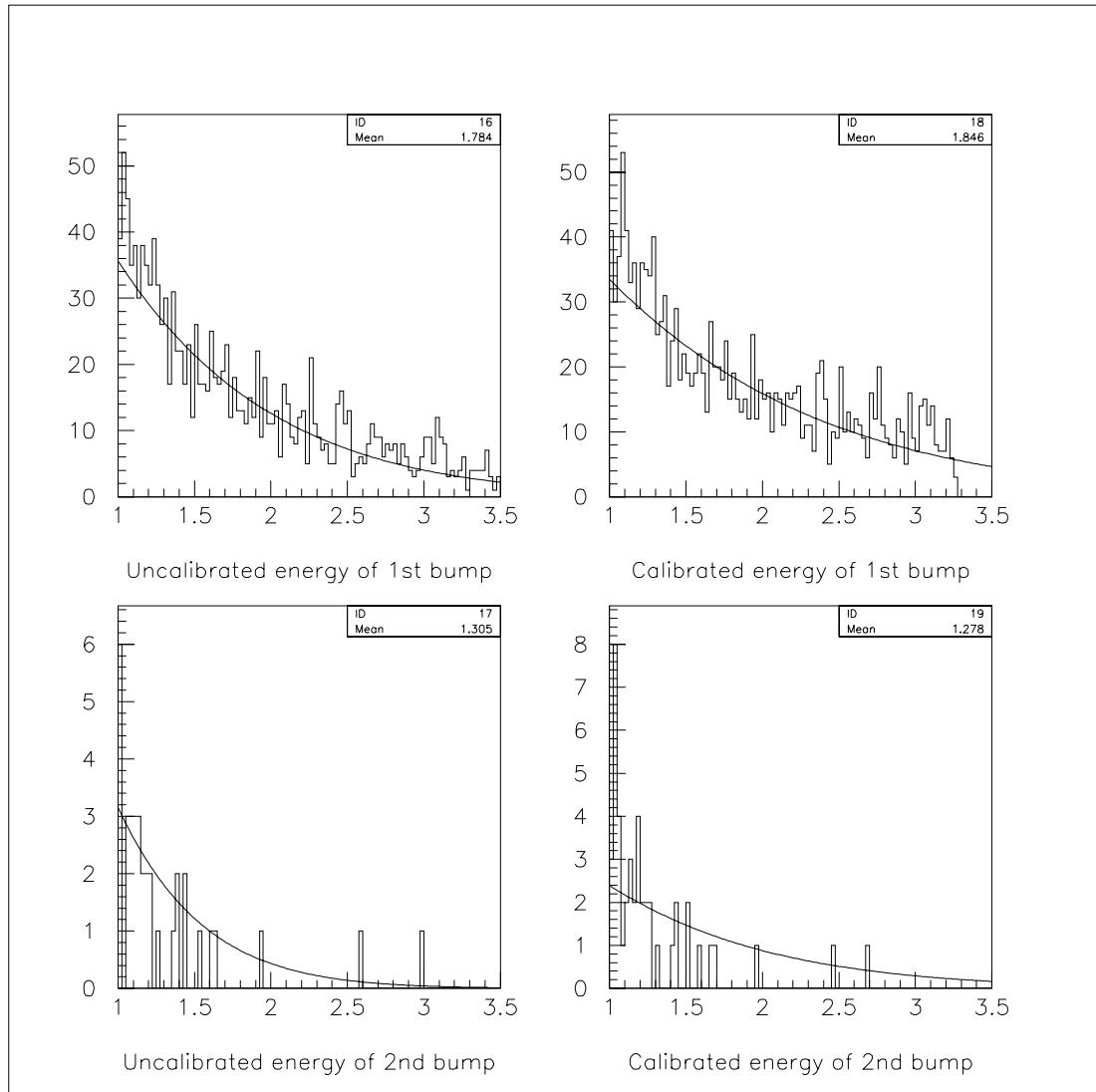
Figure 6.5: Number of entries vs. bump energy for bumps 1 and 2
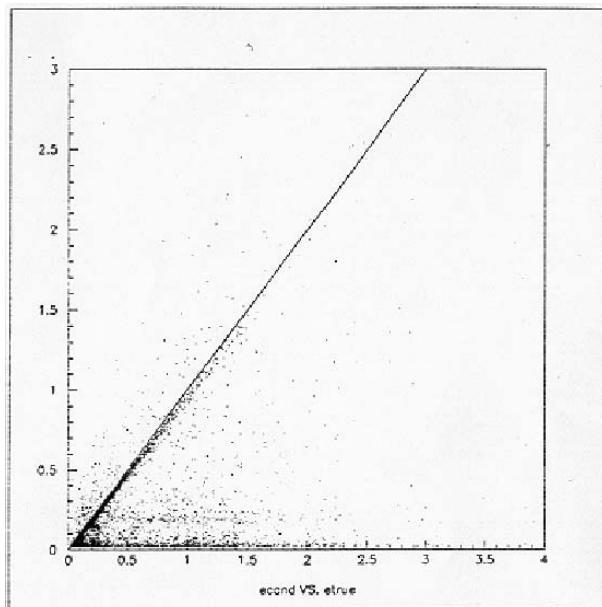
Figure 6.6: Photon candidate energy vs. MC truth energy
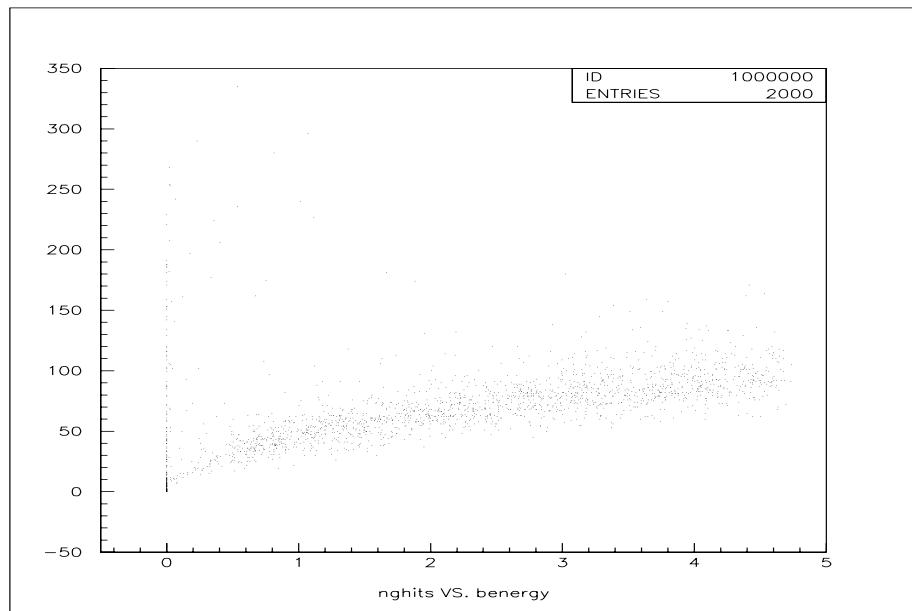

Figure 6.7: Bump energy hitmap
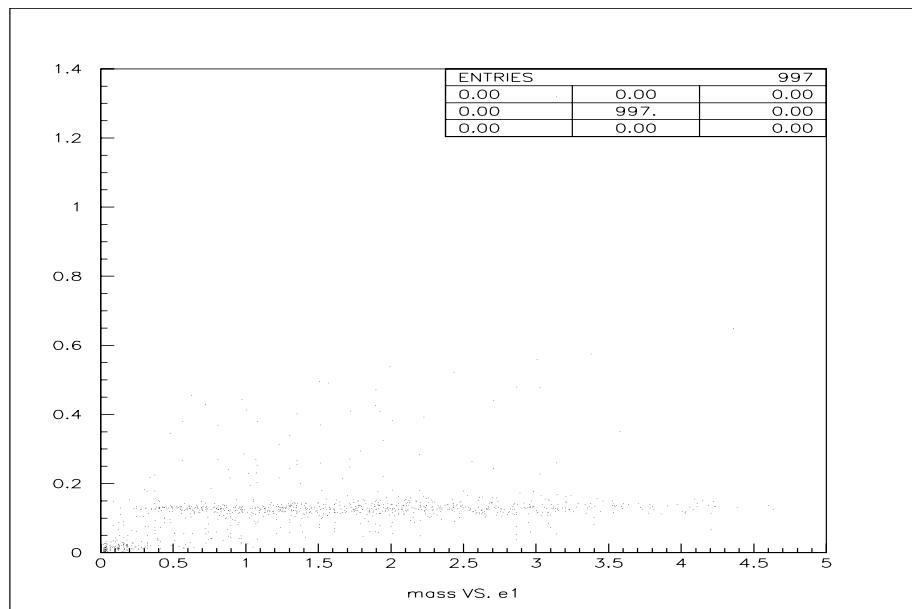
Figure 6.8: π^0 mass as a function of bump energy
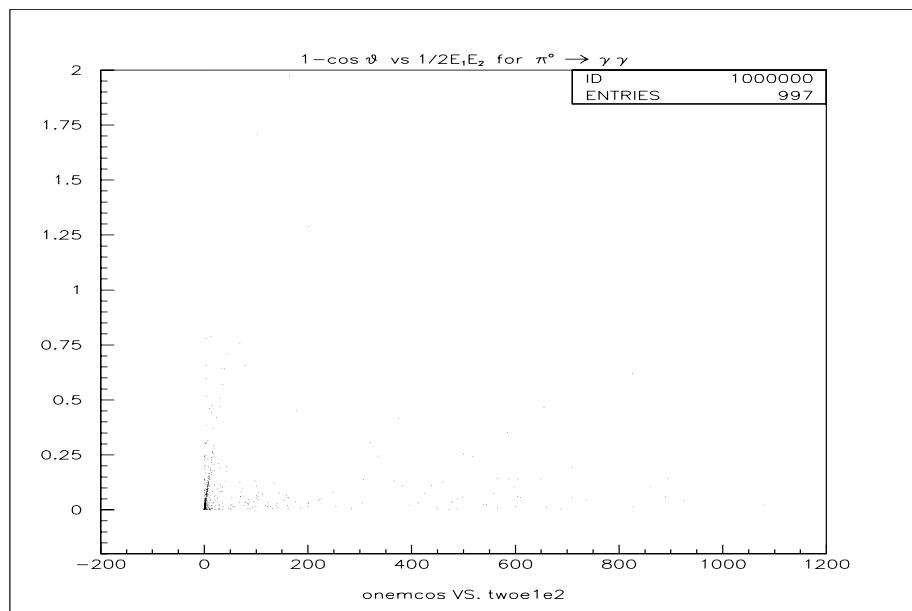

Figure 6.9: Linear plot of mass-squared

| ID			100
0.00		64.0	71.0
0.00		735.	127.
0.00		0.00	0.00
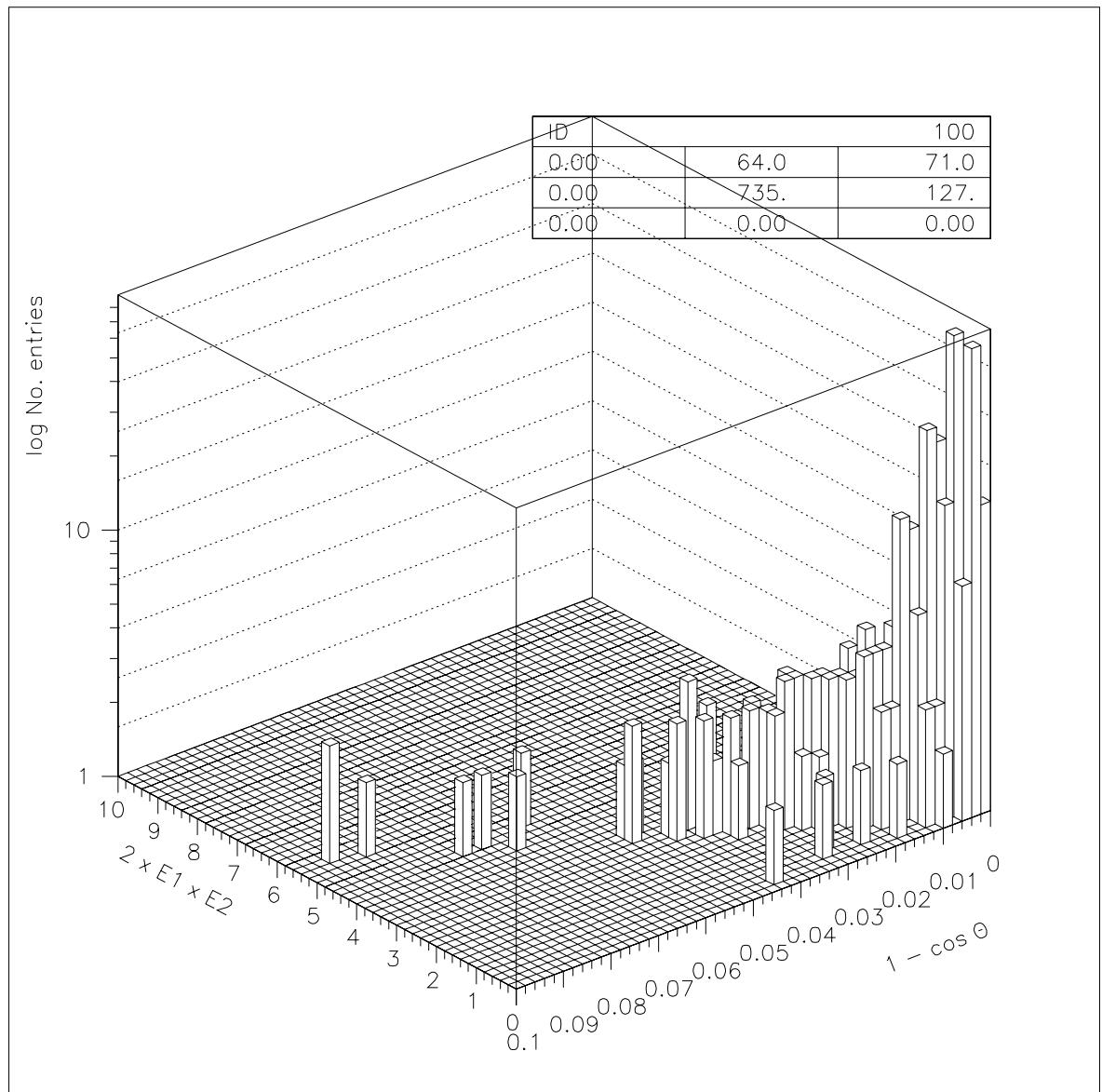
Figure 6.10: Lego plot for peak-finding and mass measurement
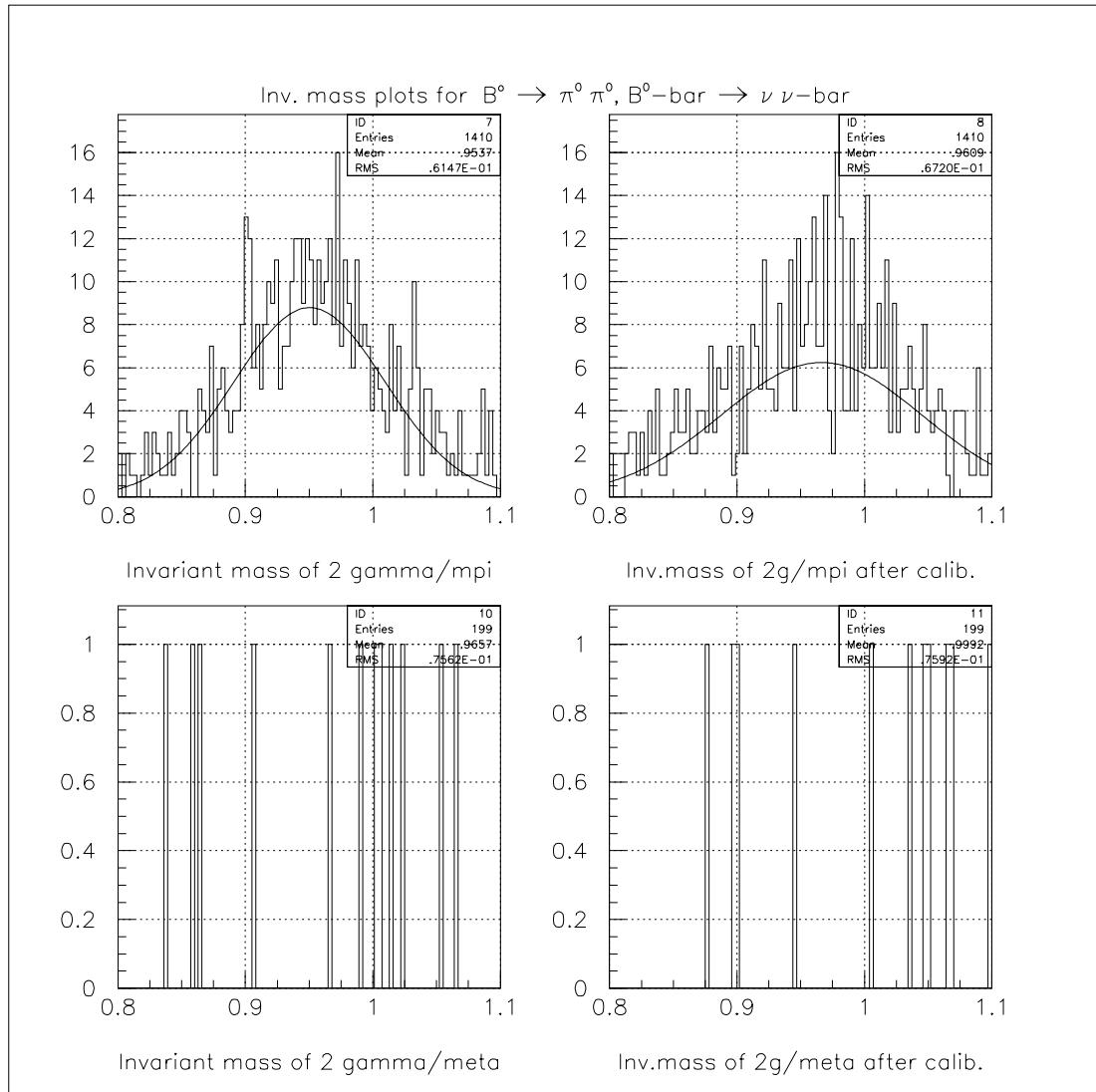
Figure 6.11: $B^0 \rightarrow \pi^0\pi^0$
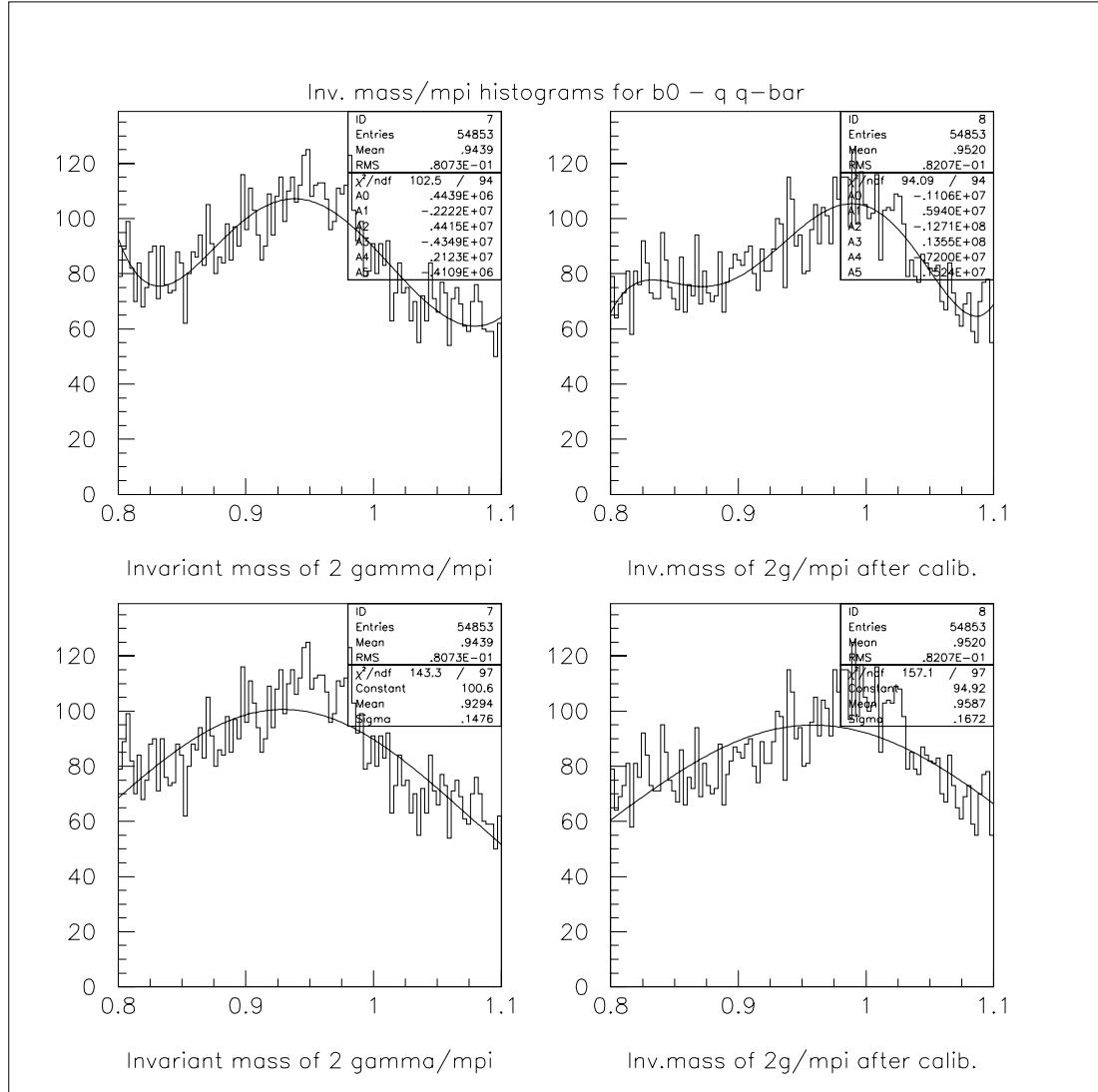
Figure 6.12: $\Upsilon(4s) \to Q\bar{Q} \to X+$ background events
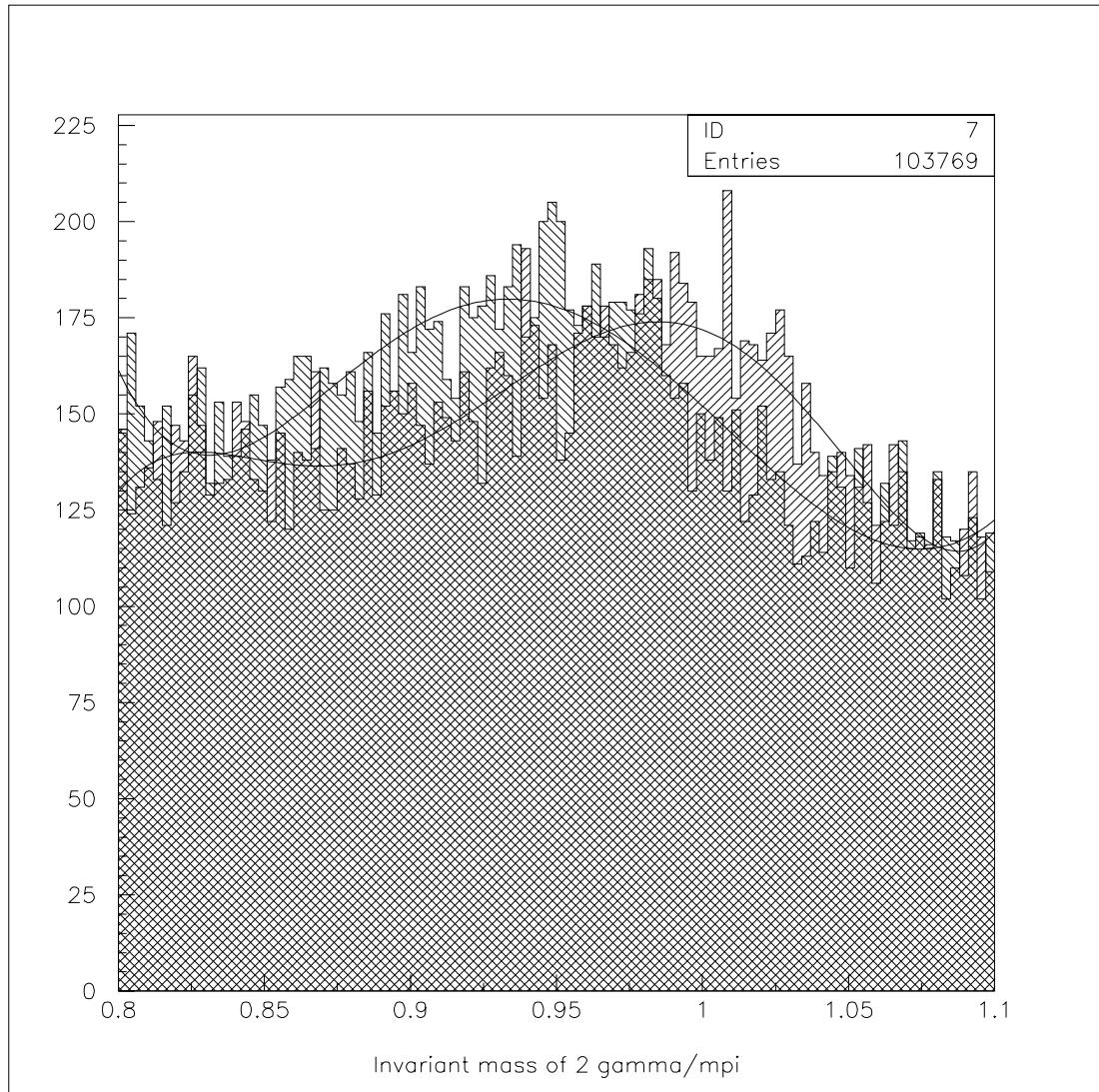
Figure 6.13: Background results without charged rejection
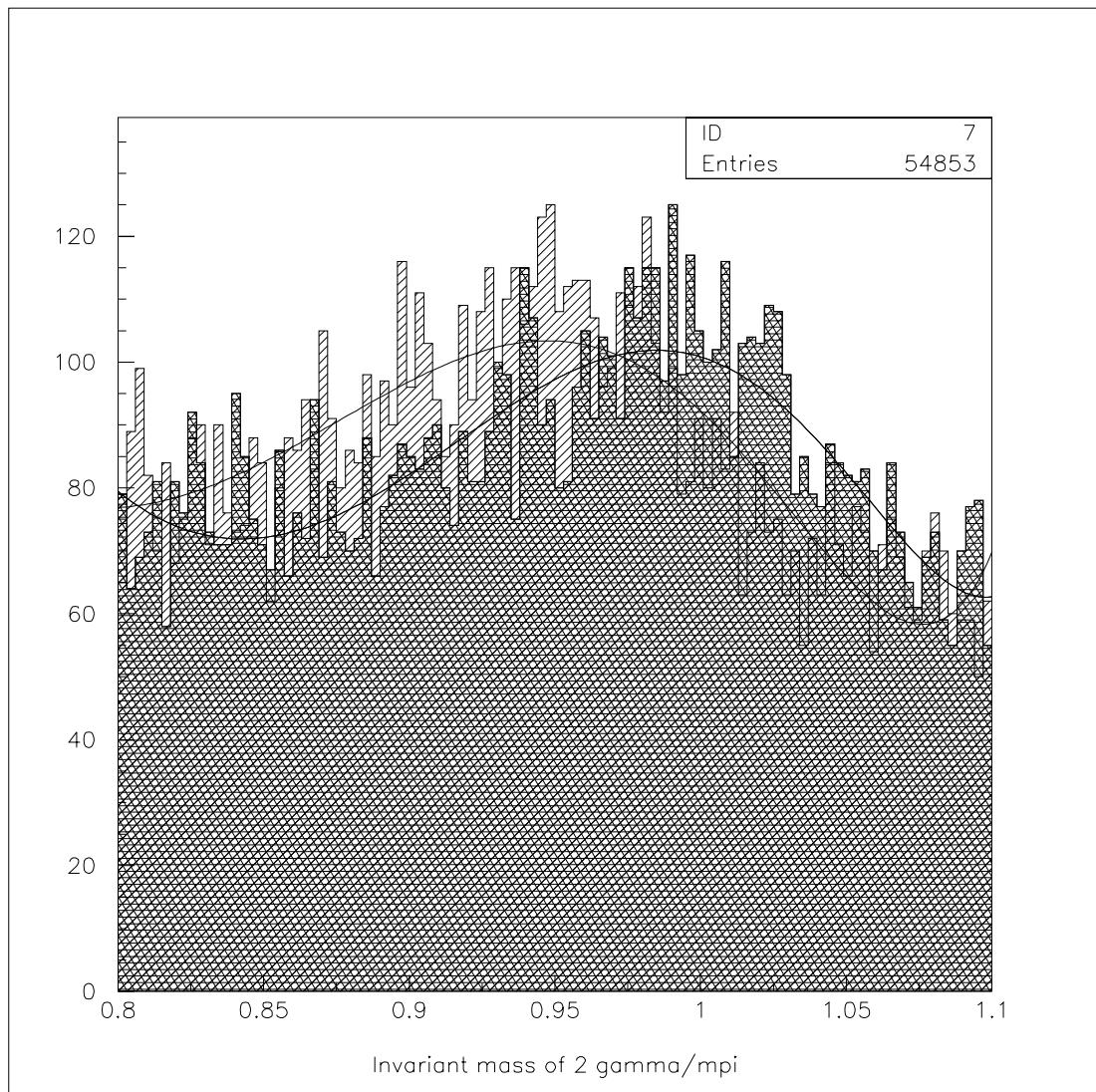
Figure 6.14: Background results with charged rejection

Bibliography

[1] Halzen, F. and Martin, D., "Quarks and Leptons", (section 12.12), Wiley and Sons, (1984).

[2] The *BaBar* Collaboration, Technical Design Report, (1995).

[3] Huet, P. and Nelson, A., "*CP* violation in Electroweak Baryogenesis in Extensions of the Standard Model", submitted to *Physics Letters B*.

[4] Stone, S., Nir, Y. and Quinn, H., "B Decays (2nd Edition): Theory of *CP* Violation in B Decays", World Scientific, (1994), 520-550.

[5] R. Godang et. al., The CLEO-II Collaboration, *Phys. Rev. Lett.* **80** 3456 (1998).

[6] Eerola, P., "B-Physics potential of ATLAS: an update", submitted to *Nucl. Instr. Methods* A.

[7] The *BaBar* Collaboration, (Pre-print of) The *BaBar* Book.

[8] Close, F.E., "An Introduction to Quarks and Partons", Academic Press, (1979).

[9] Fernow, R, "Introduction to Experimental Particle Physics", Cambridge University Press, (1989), 79-91.

[10] Crystal Barrel Collaboration, "Crystal Barrel Spectrometer at LEAR", *Nucl. Instr Methods*, **A321** (1992), 69-108.

[11] Bernet, R. et. al., "Calibration and Monitoring for the *BaBar* Calorimeter", *BaBar* Note # 363 (1996), 1-24.

[12] Skovpen, Y., "Calibration of Calorimeter with Bhabha Events", *BaBar* Note # 356 (1997), 1-16.

[13] Pohl, I., "Object-Oriented Programming Using C++", Benjamin/Cummings, (1993), chapter 1.

[14] Kreyszig, E., "Advanced Engineering Mathematics", Wiley and Sons, (1988), 971-975.

[15] The CLEO II Collaboration, "The CLEO II detector", *Nucl. Instr. Methods*, **A320** (1992), 66-113.

[16] Crystal Barrel Collaboration, "Crystal Barrel Spectrometer at LEAR", *Nucl. Instr Methods*, **A321** (1992), 69-108.

[17] Heltsey, B.K., private communication.

[18] Bukin, A., private communication.

[19] The *BaBar* Collaboration, Technical Design Report, (1995).

[20] Barlow, R. J., private communication.

[21] Physical Review D: Particles and Fields. The American Physical Society (1996).

[22] Crystal Barrel Collaboration, "Crystal Barrel Spectrometer at LEAR", *Nucl. Instr Methods*, **A321** (1992), 69-108.

[23] Budkin, A. and Marsiske, H., "Absolute Energy Calibration of the *BaBar* Calorimeter using pi0's", *BaBar* Note # 339 (1997).